Comparing Raman and NanoSIMS for heavy water labeling of single cells

Running title: Comparing Raman and NanoSIMS

George A. Schaible [1,2], John B. Cliff [3#], Jennifer A. Crandall [2,4], Jeremy J. Bougoure [2], Joseph Atwood [5], and Roland Hatzenpichler [1,2,4,6*]

[1] Department of Chemistry and Biochemistry, Montana State University, Bozeman, MT 59717
[2] Center for Biofilm Engineering, Montana State University, Bozeman, MT 59717
[3] Environmental Molecular Sciences Laboratory, Pacific Northwest National Laboratory, Richland, WA 99354
[4] Department of Microbiology and Cell Biology, Montana State University, Bozeman, MT 59717
[5] Department of Agricultural Economics and Economics, Montana State University, Bozeman, MT 59717
[6] Thermal Biology Institute, Montana State University, Bozeman, MT 59717
[#] Current address: National Security Directorate, Oak Ridge National Laboratory, Oak Ridge, TN

* Correspondence to roland.hatzenpichler@montana.edu. phone: +1-406-994-5469. 111 Chemistry and Biochemistry Building. Montana State University, Bozeman, MT 59717. USA

ORCID: GAS, 0000-0002-1031-4682. JBC, 0000-0002-7395-5604. JAC, 0000-0002-9051-8481. JJB, 0000-0002-4869-035X. RH, 0000-0002-5489-3444.

Conflict of interest: The authors declare no conflict of interest.

Funding source: NIH 1R35GM147166-01

Keywords: Cellular heterogeneity, D_2O, cell activity, single cell microbiology, technique comparison, Raman, NanoSIMS

Abstract

Stable isotope probing (SIP) experiments in conjunction with Raman microspectroscopy (Raman) or nano-scale secondary ion mass spectrometry (NanoSIMS) are frequently used to explore single cell resolved metabolic activity in pure cultures as well as complex microbiomes. Despite the increasing popularity of these techniques, no study has yet compared results from isotope incorporation measurements using both Raman and NanoSIMS directly on the same cell. This knowledge gap creates uncertainty about the comparability of single cell SIP data generated independently using these techniques. In this study, we conducted a comparative analysis of 543 *Escherichia coli* cells grown in M9 minimal medium in the absence or presence of heavy water (^2H_2O) at single cell resolution using correlative Raman and NanoSIMS measurements. For the first time, we were able to establish the extent of data equivalence, allowing for comparisons between the two approaches. Utilizing the dataset from this study, we examined the effectiveness of preprocessing techniques and optimal wavenumbers for analyzing Raman spectra, along with identifying the ideal masses for NanoSIMS analysis of cells incubated in the presence of ^2H_2O. We make recommendations for approaches to analyzing and comparing data using both or either of these techniques. We anticipate that the findings presented herein will enhance the comparability of studies

employing either technique and ultimately contribute to the establishment of a standardized framework within the field.

Importance

Accurate and reliable measurements of cellular properties are fundamental to understanding the function and activity of microbes. This study addresses to what extent Raman microspectroscopy and nano-scale secondary ion mass spectrometry (NanoSIMS) measurements of single cell anabolic activity can be compared. For the first time, we study the relationship of the incorporation of a stable isotope (^{2}H through incorporation of $^{2}H_2O$) as determined by the two techniques and calculate a correlation coefficient to support the use of either technique when analyzing cells incubated with $^{2}H_2O$. The ability to discern between the comparative strengths and limitations of these techniques is invaluable in refining experimental protocols, enhancing data comparability between studies, data interpretation, and ultimately advancing the quality and reliability of outcomes in microbiome research.

Introduction

Microbial activities and cellular interactions drive human health, global biogeochemical cycles, and ecosystem function. Stable isotope probing (SIP) is a particularly powerful approach to studying microbial function and is widely used in microbiology (1-5). By measuring the incorporation of heavy isotopes (*e.g.*, ^{2}H, ^{13}C, ^{15}N, ^{18}O) into biomass, it is possible to assess the activity and physiology of individual cells at a microbially-meaningful spatial resolution, enabling a comprehensive understanding of community dynamics (4). While SIP can be applied to all assimilatory pathways, heavy water labeling holds appeal for microbiologists due to its universal applicability, negating the need for prior knowledge of cell physiology (2). Moreover, the use of heavy water eliminates the requirement for prohibitively expensive or unavailable isotope-labeled growth substrates and avoids interference with the substrate pool of a system (1). Active microbes grown or incubated in the presence of heavy water will use deuterium (^{2}H) in lieu of hydrogen (^{1}H) during biosynthesis, resulting in active microbial community members becoming labeled with ^{2}H (6, 7). Because ^{2}H naturally occurs at very low levels (~0.016%), its environmental background is usually negligible for biological labeling studies (8, 9).

The assimilation of isotopically labeled substrates, including heavy water, into individual cells can be measured by either Raman microspectroscopy (Raman) or nano-scale secondary ion mass spectrometry (NanoSIMS). Micro-autoradiography is a cost-effective alternative but is limited to radioactive isotopes (10, 11). All three techniques can be combined with fluorescence *in situ* hybridization (FISH), which allows a direct link between cellular identity and function in complex microbiomes (3, 12-14).

Raman is a non-destructive spectroscopic technique based on the inelastic scattering of light. It can be applied directly to environmental samples with minimal preparation (15), allowing for real-time monitoring of metabolic changes of single cells (16). By exciting molecular bond vibrations, Raman elucidates the spatial distribution of specific biomolecules, such as lipids, proteins, and nucleic acids within cells and/or communities on a sub-micrometer scale (3, 15). Incorporation of stable isotopes into biomolecules changes the vibrational energy of excited molecules through the increased molecular mass, inducing a red shift towards smaller wavenumbers (15, 17). While Raman requires little or no sample preparation, the technique suffers from low sensitivity (~10% ^{13}C, ~10% ^{15}N, and ~0.2% ^{2}H cellular replacement (15, 17, 18)) and low signal-to-noise ratio as compared to mass spectrometry. However, carbon-deuterium ($^{12}C^{2}H$) bonds are reliably detected in Raman spectra by a characteristic peak shift of the abundant $^{12}C^{1}H$ peak into the mostly

Raman-silent region (1,800-2,800 cm^{-1}) of the cellular spectrum making Raman analysis well suited for deuterium SIP analysis in single cells (2).

NanoSIMS uses a focused ion beam to produce secondary ions from a sample surface that are subsequently analyzed via a double focusing mass spectrometer to attain spatially resolved elemental and isotopic information (19, 20). Although NanoSIMS is capable of detecting isotopes at a much greater sensitivity and spatial resolution (≥50 nm) than Raman, it is destructive to the sample and provides limited molecular information (21). Furthermore, it can suffer from recombination of atoms during ion beam sputtering, which may result in misinterpretation of results. However, in the case of ^{13}C- and ^{15}N-labeling of biological materials, recombination is not thought to affect the general interpretation of NanoSIMS results (21).

Both Raman and NanoSIMS are powerful tools for studying the structure, function, and interactions of microbes on a single-cell or community level (3, 20). Studies have successfully applied both techniques in tandem, including analysis of deposition of organic material in diatom fossils (22), SIP experiments of microbial cells recovered from soils and sediments (23, 24), and *in vitro* SIP of microbial cells for sorting (2). However, to the best of our knowledge, only two studies ever applied Raman and NanoSIMS on the same cells (24, 25), and a comprehensive and direct comparison of these techniques is currently unavailable, which makes it difficult to compare and interpret results generated by these techniques.

To address this shortcoming, we employed SIP on *Escherichia coli* using deuterium oxide (^2H_2O) and compared results of Raman and NanoSIMS based measurements of 543 individual cells. We demonstrate strong correlation of these measurements, enabling the corroboration of data obtained from either technique alone. This data set also enabled an investigation into the pre-processing of Raman data and the ideal mass measurements used for NanoSIMS, providing insights on how to best optimize the methodology when using either technique for ^2H incorporation measurements. In addition, we investigated a statistical approach for calculating wavenumber ranges for $^{12}C^2H$ measurements using Raman. Considering that both Raman and NanoSIMS possess unique strengths and limitations, the drawbacks of one technique can be compensated by the other, thereby granting a more comprehensive insight into biological samples at a micrometer scale (24). Ultimately, this comparative investigation contributes to refining our understanding of the comparability of Raman and NanoSIMS data and lays the foundation for future integrated approaches of correlative SIP-Raman-NanoSIMS analyses.

Results

Stable isotope probing

We employed our recently developed correlative workflow (24) for the study of single *E. coli* K12 cells that had been grown in unamended media (0% ^2H_2O) or media amended with either 15%, 30%, or 50% ^2H_2O. Cells were collected during mid-logarithmic growth (Fig. 1 and S1), fixed with PFA to preserve cells and inhibit change in ^2H content, immobilized on a stainless-steel coupon, stained with 4',6-diamidino-2-phenylindole (DAPI, necessary for visualization during next step), and regions of interest (ROIs) mapped using laser dissection microscopy (Fig. S2). All cells within the ROIs were then first analyzed by Raman before NanoSIMS measurements were performed.

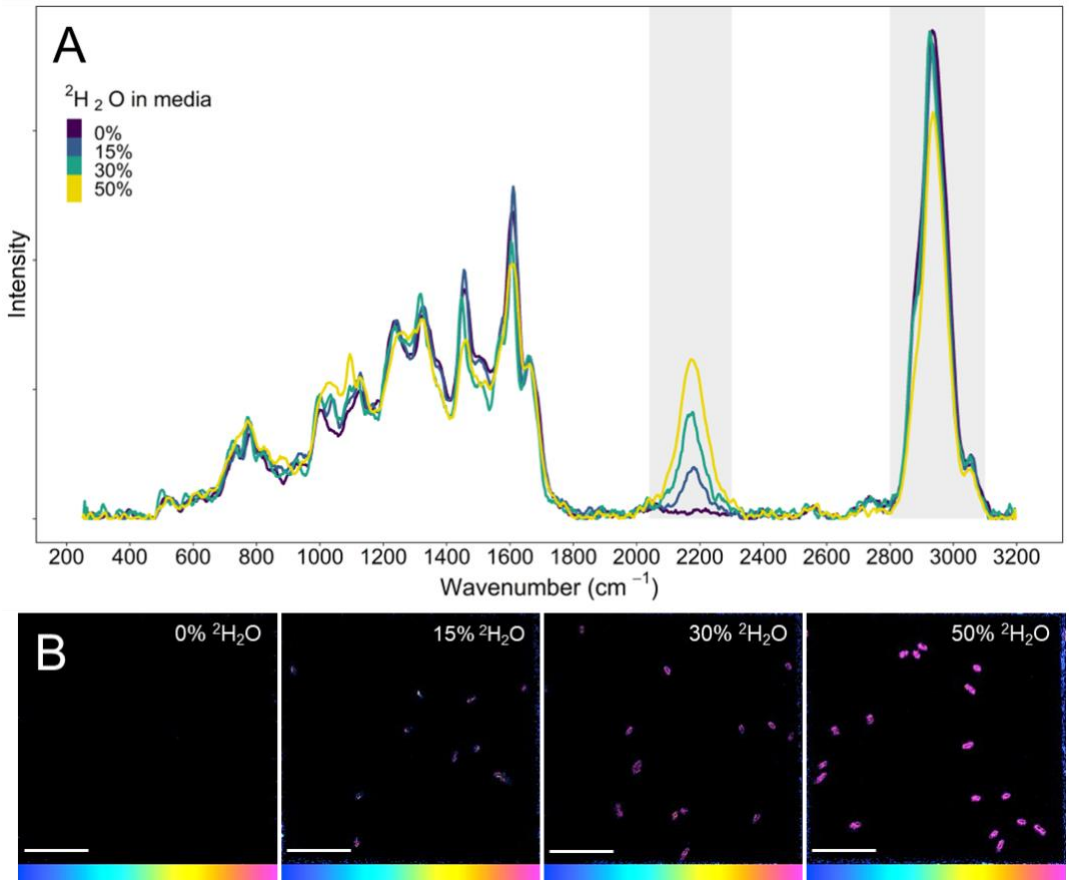

Fig. 1. Exemplary Raman spectra and NanoSIMS images illustrating the uptake of ^{2}H-label by *Escherichia coli* K12 cells after incubation in media with varying percentages of ^2H_2O. **A** The characteristic $^{12}C^2H$ and $^{12}C^1H$ regions are shaded in gray. **B** $^{12}C_2{}^2H/^{12}C_2{}^1H$ mass ratio NanoSIMS images. All isotope fraction images are on the same scale (0-30 atom %). Scales bars are 5 µm.

Pre-processing of Raman spectra

Currently, there is no standard method for the pre-processing of Raman spectra (15), despite compelling evidence demonstrating the influence of processing procedures on data outcomes (26). Optimizing the workflow by testing various pre-processing procedures on Raman spectra before selecting a method is recommended to minimize information loss in the spectra (27, 28). To address the lack of standardization in pre-processing methods, we systematically tested various methods on our Raman spectra to optimize our spectra processing methodology.

Raman spectra spanning 250-3,200 cm^{-1} were acquired from individual cells within the ROIs. To test if peaks in the fingerprint region of spectra (ca. 700-1,800 cm^{-1}) induce a leveraging effect during smoothing and baselining of the spectra, spectra were analyzed as a whole (250-3,200 cm^{-1}) or were truncated to 1,800-3,200 cm^{-1}, as was previously suggested (27, 29). All spectra were smoothed using a Savitzky-Golay smoothing algorithm, which applies a moving window based on a local polynomial fitting procedure, to reduce the signal to noise ratio (30). Excessive smoothing of spectra can result in the loss of genuine Raman bands thereby producing inaccurate spectra. To avoid this, we used a 2nd degree polynomial with a window size of 11 to ensure important peaks were preserved in spectra across all samples. Next, several commonly

applied baselining methods were tested to identify if background correction influences the final calculation of ^{2}H content of the *E. coli* cells.

The first baselining method applied was asymmetric least squares (ALS), an iterative method that uses asymmetric weighting to adjust the extent in which data influence baselining (31). The second method used was a polynomial fit, where a polynomial of nth degree (we used a 2nd degree polynomial) can be fit to both the spectra and the baseline subtracted to remove background (32). The third method tested was a frequency differentiated non-linear digital filter, commonly referred to as "rolling ball", which is equivalent to rolling a ball with a given ball diameter (*i.e.*, window size) below the spectra and removing the background below the points the ball touches (33). The fourth and final method tested was statistics-sensitive non-linear iterative peak-clipping (SNIP), a process that compresses the data using a log square root operator followed by iterative evaluations using a clipping window, after which the data is transformed back using the inverse log square root (34). In contrast to the other baselining methods, SNIP does not lead to distortions of the baseline at the edges of the spectral interval (27).

Prior to determining the efficacy of the baselining methods, each spectrum was normalized using sum normalization to maintain relative proportions of peaks for comparisons. Next, the ^{2}H incorporation into cells was quantified by calculating the ratio between the area under the curve (AUC) of the $^{12}C^{2}H$ (2,040-2,300 cm^{-1}) and the $^{12}C^{1}H$ (2,800-3,100 cm^{-1}) region of each spectrum (Fig. 1A). The AUC was determined by drawing a linear baseline between the interval of wavenumbers and numerically integrating the area above the line and below the curve using the trapezoidal rule (Fig. S3). The ^{2}H content was then used to compare the baselining methods for both truncated spectra (1,800-3,200 cm^{-1}) and whole spectra (250-3,200 cm^{-1}), and the r-squared value used to determine the fit of each model (Fig. S4).

There was no statistically significant difference between the truncated and whole spectra or between the baselining methods, except for spectra baselined using the rolling ball method (Fig. S5, Table S1). This indicates that the baselining method had little effect on ^{2}H calculation from Raman spectra of *E. coli*. This could be due to the low background observed in a pure culture as compared to an environmental sample and the low natural fluorescence of *E. coli*, resulting in minimal background subtractions from the data. We elected to use the SNIP baselining method for our analysis because this method has minimal distortion on data at both ends of the spectrum and has previously been used in single cell SIP-Raman studies (2, 23, 35).

NanoSIMS analyses

The next step in our workflow was to examine the ^{2}H content of each cell that had previously been measured by Raman using NanoSIMS (Fig. 1B). Historically, analysis of ^{2}H uptake in cells by NanoSIMS has been performed using either the mass ratio of $^{2}H/^{1}H$ (24, 36, 37), $^{12}C^{2}H/^{12}C^{1}H$ (2, 38), or $^{16}O^{2}H/^{16}O^{1}H$ (2, 39). To explore if the choice of mass ratio leads to different interpretations of the ^{2}H-content of cells, we measured the $^{2}H/^{1}H$, $^{12}C^{2}H/^{12}C^{1}H$, and $^{12}C_{2}{}^{2}H/^{12}C_{2}{}^{1}H$ mass ratios using NanoSIMS and compared them to Raman data of the same cells. CH^{-} and $C_{2}H^{-}$ have relatively higher ion yields compared to H; however, higher mass resolving power is required to acquire these signals without overlapping interferences (40, 41). Although the use of $^{12}C^{2}H/^{12}C^{1}H$ and $^{12}C_{2}{}^{2}H/^{12}C_{2}{}^{1}H$ in polymer films and charcoal has been explored using high mass resolving power, these studies have used a high primary beam current and relatively low spatial resolution (40, 41), and/or nonstandard instrument configurations to achieve optimum results (41). Because we wanted to perform spatially resolved isotopic analyses on single microbes, we chose to use a lower primary beam current with higher spatial resolution (~120 nm) along with standard mass resolving power for these experiments.

Because NanoSIMS precision is ultimately limited by total ion counts (44), it is interesting to note that, on average, $^{12}C_2{}^1H$ counts were roughly five times that of $^{12}C^1H$ counts for individual cells (Fig S6). This is at least in part due to the greater electron affinity of C_2H compared with CH (42, 43). Thus, in theory, the minimum average internal uncertainty (based on counting statistics; (44)) should be roughly 2.2 times higher for $^{12}C^2H/^{12}C^1H$ than for $^{12}C_2{}^2H/^{12}C_2{}^1H$ (44). Table S2 summarizes these data. Except for cells grown without added ^2H_2O, data are largely consistent with these expectations. Cells grown in 15%, 30%, and 50% ^2H_2O had an average internal standard deviation (SD) of 2.28 for C^2H/C^1H estimates relative to $C_2{}^2H/C_2{}^1H$ (n = 230). The corresponding comparison of average external uncertainties are slightly lower (SD = 1.92) and are consistent with expectations of external uncertainties being limited by internal uncertainties. The average relative internal and external uncertainties for the same ion pairs for cells grown without ^2H_2O are 9.60 and 11.83 respectively (n = 86, Table S2). We attribute the higher uncertainties to the presence of difficult to resolve and highly variable isobaric interferences (40).

Two observations stand out from the $^2H/^1H$ measurements. First, the background associated with cells grown without ^2H_2O was significantly lower than measurements using the CH^- and C_2H^- ions. Second, the slope of the regression line for the % ^2H_2O in the growth medium versus NanoSIMS $^2H/^1H$ data is significantly lower than the corresponding regressions for the other ion pairs (Fig. S7). The lower background can be attributed to the relative absence of difficult to resolve isobars. Assuming a value for the natural abundance $^2H/H$ of 0.000156 (VSMOW), the slope of the regression of $^2H/^1H$ versus the concentration of ^2H_2O in the growth media (in %) is consistent with an instrumental mass fractionation (IMF) of ~ -380 ‰ compared with the regressions for $^{12}C^2H/^{12}C^1H$, and $^{12}C_2{}^2H/^{12}C_2{}^1H$. This fractionation is in the range of values reported for SIMS analyses in the past (45). Because $^2H/^1H$ measurements were performed in a different analytical session with different instrument tuning parameters to account for the order of magnitude difference in mass, we cannot directly compare relative uncertainties with the other ion pairs. However, we summarize the relative internal and external uncertainties of $^2H/^1H$ under the assumption that the average cell $^2H/^1H$ ratios of the cells are similar between analytical sessions (Table S3). Although this assumption is likely true, as discussed below, artefacts peculiar to the NanoSIMS ionization process likely means that different populations of ^2H were sampled and counted.

Intriguingly, we found a statistically significant difference ($p < 0.005$) between each pair of mass ratios used to measure the ^2H content of cells at each concentration of ^2H_2O in the media (Fig. S8). On average, the $^{12}C^2H/^{12}C^1H$ ratio indicated the highest apparent relative ^2H content in cells, the $^{12}C_2{}^2H/^{12}C_2{}^1H$ ratio indicated the second highest, and the $^2H/^1H$ ratio showed the lowest. This discrepancy was likely not sample-specific as the $^{12}C^2H/^{12}C^1H$, and $^{12}C_2{}^2H/^{12}C_2{}^1H$ mass ratios were concurrently measured on the same cells, and the $^{12}C_2{}^2H/^{12}C_2{}^1H$ yielded robust count numbers (Fig. S6). Rather, the differences were likely due to some combination of sampling different ^2H populations associated with the individual cell, different IMF factors, and variable atomic mixing during the sputtering process (22). The $^2H/^1H$ mass ratio was measured on separate cells due to the need to change the calibration of the instrument to detect the low mass. Additionally, linear regressions of the data showed that the slope of the $^2H/^1H$ data was less (~0.1) than the $^{12}C^2H/^{12}C^1H$, and $^{12}C_2{}^2H/^{12}C_2{}^1H$ data (Fig. S7). Due to the variations in apparent ^2H content of cells between the different mass ratios, we made our Raman-NanoSIMS comparisons using all three mass ratios.

Because DAPI staining was necessary to visualize cells during etching of the sample surface with the laser dissection microscope used for cell mapping, we investigated the effect of DAPI on the dilution of the ^2H signal. Addition of hydrogen-rich chemicals, such as the fixatives paraformaldehyde (PFA) and ethanol or DNA-staining chemicals such as DAPI and SYBR dyes, can result in a dilution of isotopes in cells (39). The comparison of cells that had been incubated with ^2H_2O and either underwent DAPI-staining or had no

DAPI treatment, revealed an average decrease of 12.8% percent of total ^{2}H signal when cells are treated with DAPI (Fig. S9). This dilution of ^{2}H is not surprising considering that DAPI contains fourteen hydrogen atoms per molecule and binds to twelve base pairs along the minor groove in DNA (46), suggesting that in the approximately 4.6 Mb long chromosome of *E. coli* K12 there could be an additional 5.4 x 10^{6} ^{1}H deposited by DAPI staining per chromosome copy. Although this number is likely inflated due to the specific binding of DAPI to adenine-thymine rich regions in the minor groove of DNA, which are not present in every full turn of the minor groove (46), this example serves to highlight the effect DAPI can have on single cell isotope measurements. If working with environmental microbes that have low activity, pretreatment of cells should be limited as much as experimentally possible (39).

Single-cell comparison of Raman and NanoSIMS

A comparison of the Raman spectra (analyzed using the 2040-2300 cm^{-1} wavenumber range for ^{2}H calculations) and NanoSIMS measurements (for $^{2}H/^{1}H$, $^{12}C^{2}H/^{12}C^{1}H$, and $^{12}C_2{}^{2}H/^{12}C_2{}^{1}H$ mass ratios) of 543 cells revealed a high degree of comparability between the two techniques (Fig. 2). The highest correlation of labeling percentages determined by Raman and NanoSIMS were found using the $^{12}C_2{}^{2}H/^{12}C_2{}^{1}H$ mass ratio (0.98 r-squared). The $^{2}H/^{1}H$ and $^{12}C^{2}H/^{12}C^{1}H$ mass ratios showed equal correlation (0.97 r-squared) to the Raman results although the NanoSIMS data for the $^{2}H/^{1}H$ had a much lower degree of spread for the 0% $^{2}H_2O$ incubations as compared to $^{12}C^{2}H/^{12}C^{1}H$. Considering the slope of the models, each comparison had a slope >1, indicating that Raman estimated a higher amount of deuterium in the cells than NanoSIMS. This discrepancy was the greatest with the $^{2}H/^{1}H$ mass ratio for which the slope of the model was 1.5. Furthermore, the y-intercept was near-zero for $^{2}H/^{1}H$ and $^{12}C_2{}^{2}H/^{12}C_2{}^{1}H$ while the $^{12}C^{2}H/^{12}C^{1}H$ mass ratio had a y-intercept of -4.86, representative of the high estimation of ^{2}H in the cells for the 0% $^{2}H_2O$ incubation. Comparison of ^{2}H content in each cell based on $^{2}H_2O$ incubations as measured by NanoSIMS each or Raman revealed statistically significant differences between the techniques (Fig. 3). The $^{12}C_2{}^{2}H/^{12}C_2{}^{1}H$ mass ratio was not significantly different from the Raman data at the 0% and 15% $^{2}H_2O$ incubations.

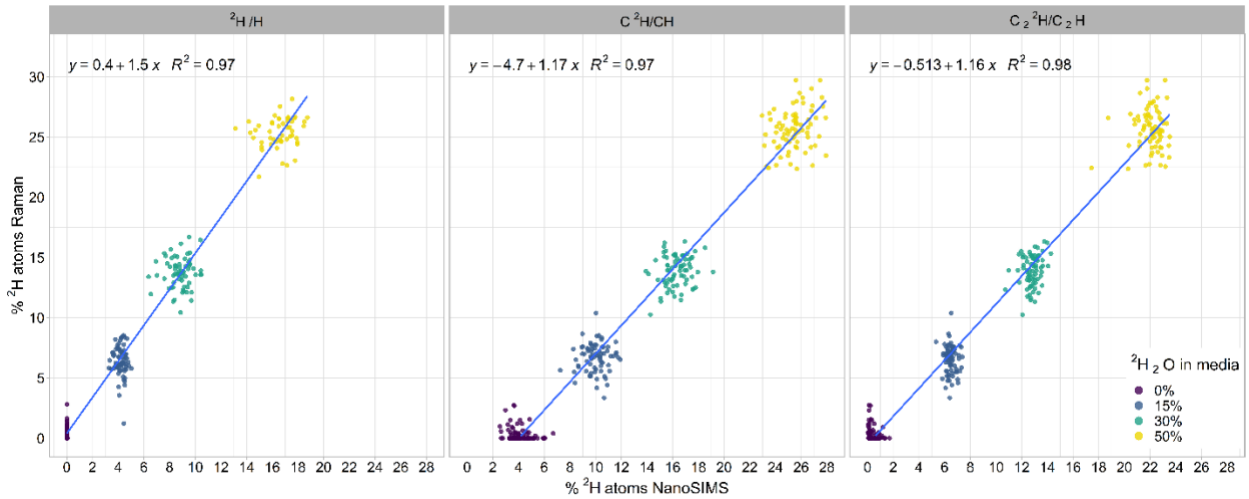

Fig. 2. Single cell comparison of the ^{2}H content of cells as measured by Raman and NanoSIMS using specific mass ratios. Each dot represents a single cell analyzed with both techniques for different $^{2}H_2O$ concentrations in the culture medium. The linear model equation and fit (blue line) is shown for each comparison of Raman to NanoSIMS regarding the specific mass ratios. In regard to y-intercept, slope, and r-squared, a mass ratio of $C_2{}^{2}H/C_2{}^{1}H$ is best used for comparisons to Raman.

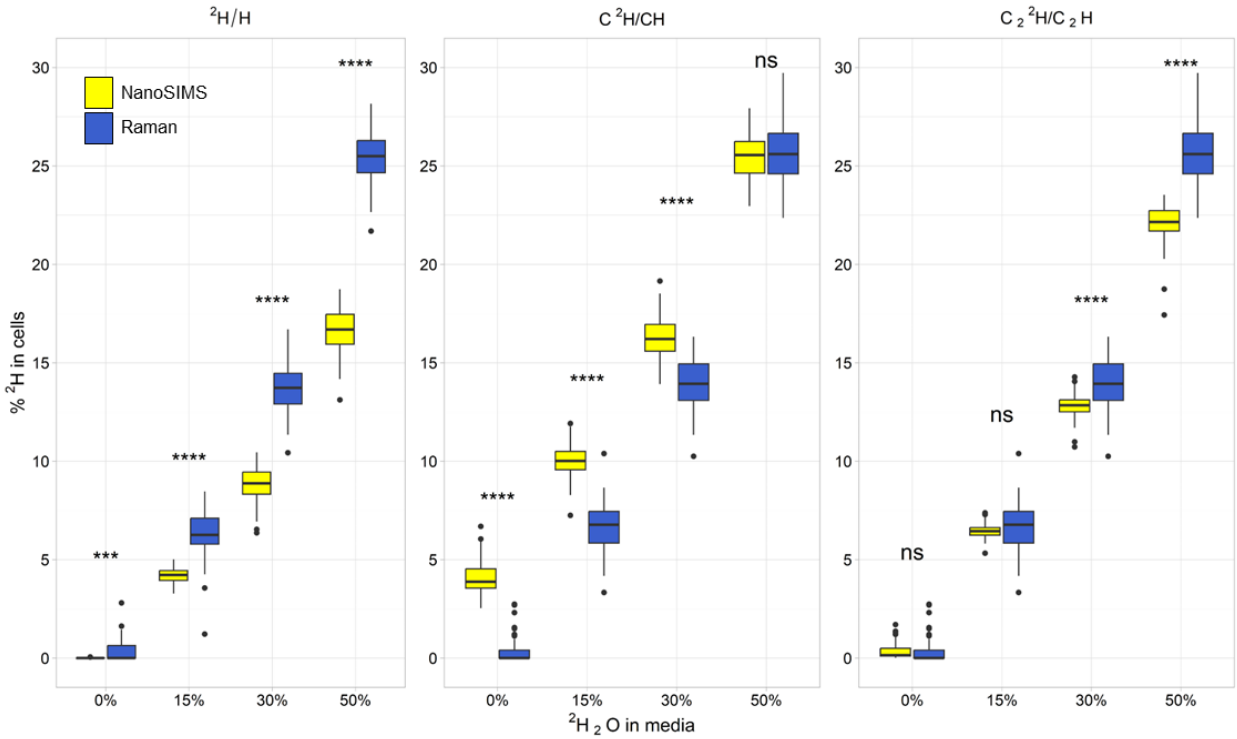

Fig. 3. Comparison of 2H atom percent as measured by Raman (2040-2300 cm^{-1} wavenumber range for ^{2}H peak) and NanoSIMS using the three different mass ratios. A higher ^{2}H content was measured by Raman as compared to the NanoSIMS ^{2}H/^{1}H mass ratio measurements. The opposite is true for the C^{2}H/C^{1}H mass ratio for which Raman measures a lower ^{2}H content than NanoSIMS. The C$_2$^{2}H/C$_2$^{1}H mass ratio had more comparable results to Raman for the 0% and 15% ^2H_2O incubations but measured a lower ^{2}H content than Raman for the 30% and 50% incubations. Because the C$_2$^{2}H/C$_2$^{1}H mass ratio contains the least statistically relevant difference to the Raman data, we recommend using this mass when comparing NanoSIMS and Raman measurements of ^{2}H. All statistically significant differences are shown: *** = p-value < 1.0 x 10^{-3}, **** = p-value < 1.0 x10^{-10}, ns = not significant.

Analysis of Raman wavenumber range

The use of the 2,040-2,300 cm^{-1} wavenumber range for Raman analysis of ^{2}H content in cells was originally proposed by Berry *et al.* and has since been ubiquitously applied in studies using Raman for ^{2}H incorporation (2, 15). We observed that applying the same wavenumber range uniformly to calculate ^{2}H in cells could lead to calculating the AUC of the baseline for cells with lower ^{2}H content, such as those in the 15% ^2H_2O incubation (Fig 1A and S3), potentially altering the ^{2}H values calculated for Raman. Furthermore, the destination of ^{2}H within a cell is dependent on the metabolism of the organism (*e.g.* anaerobic/aerobic and autotrophic/heterotrophic) and specific wavenumber peak can be influenced by additional available substrates in the incubation, highlighting the nuances to individual datasets (2, 47). To address this, we investigated whether an empirically deduced range of wavenumbers would yield results comparable to those obtained by NanoSIMS.

Calculation of wavenumber ranges was performed using the 128 Raman spectra for the 50% ^2H_2O data that had been processed by Savitzky-Golay smoothing, SNIP baselining, and sum normalization. The purpose of using the 50% ^2H_2O data was two-fold. First, at a higher ^2H_2O incubation concentration, the ^{2}H peak has a relatively normal distribution thereby reducing the noise that may influence the processing.

Second, using the highest concentration ensured the retention of data as analysis at lower concentrations would constrain the wavenumber range and likely result in removal of data at higher concentrations. Raman spectra were truncated to 2,000-2,400 cm^{-1} and further smoothed using a spline function (48). Spline smoothing is a nonparametric regression technique used to estimate a curve directly from noisy data without relying on specific parametric models, thus reducing the impact of inherent noise in the spectra on the wavenumber range calculations. The smoothness of the curve is influenced by the degrees of freedom (DOF) of the function, which can dramatically affect the calculation of wavenumber ranges. Because of this, we used a stepwise strategy involving various DOF to evaluate the impact of smoothing (Fig. S10). We computed the 2nd derivative from the smoothed curve to identify the inflection points (*i.e.*, where the 2nd derivative changes signs) and used the wavenumber values at which the inflection points occurred to determine the wavenumber range used to calculate the AUC (Fig. S11 and S12). This method provided a standardized approach for determining the wavenumber range used to calculate ^{2}H and revealed that the average wavenumber value should also be used for the DOF of the 128 Raman spectra analyzed (Table S4).

Using the wavenumber ranges for each DOF, the ^{2}H atom percent was calculated for the 50% $^{2}H_2O$ Raman data and compared to the canonical 2,040-2,300 cm^{-1} Raman wavenumber range as well as the NanoSIMS data (Fig. S13). Depending on the DOF used for smoothing, certain ranges of wavenumbers yielded results similar to results from NanoSIMS. Notably, the canonical 2,040-2,300 cm^{-1} wavenumber range matched best with the $^{12}C^{2}H/^{12}C^{1}H$ NanoSIMS mass ratio, suggesting that historic studies using this wavenumber range and mass ratio have yielded reliable results. Our analysis indicated that a narrower wavenumber range calculated from 10 DOF resulted in ^{2}H concentrations that were statistically indistinguishable from the $^{2}H/^{1}H$ mass ratio (Table S5). Similarly, no statistical difference was found when comparing the ^{2}H atom percent in Raman spectra analyzed using 5.57 DOF to the NanoSIMS $^{12}C_2{}^{2}H/^{12}C_2{}^{1}H$ mass ratio. Using the wavenumber ranges that resulted in highly similar ^{2}H amounts as compared to NanoSIMS masses, we calculated the ^{2}H for all cells in the 0%, 15%, 30%, and 50% $^{2}H_2O$ samples and compared them to the NanoSIMS data of the respective mass ratio (Fig. 4 and S13). Using the 2nd derivative deduced wavenumbers resulted in comparable ^{2}H values measured between the two techniques with lower statistical variance between the datasets (Table S7). Improvements in the ^{2}H atom percent equivalence between Raman and NanoSIMS were also observed with linear regressions of the individual cells for each of the $^{2}H_2O$ incubations (Fig. S14). As compared to the ^{2}H atom percent calculations using the canonical 2,040-2,300 cm^{-1} range shown in Figure 2, wavenumber ranges calculated using the 2nd derivative approach had closer to 1, suggesting a stronger linear correlation between the data when employing wavenumber ranges calculated using the second derivative approach (Table S8).

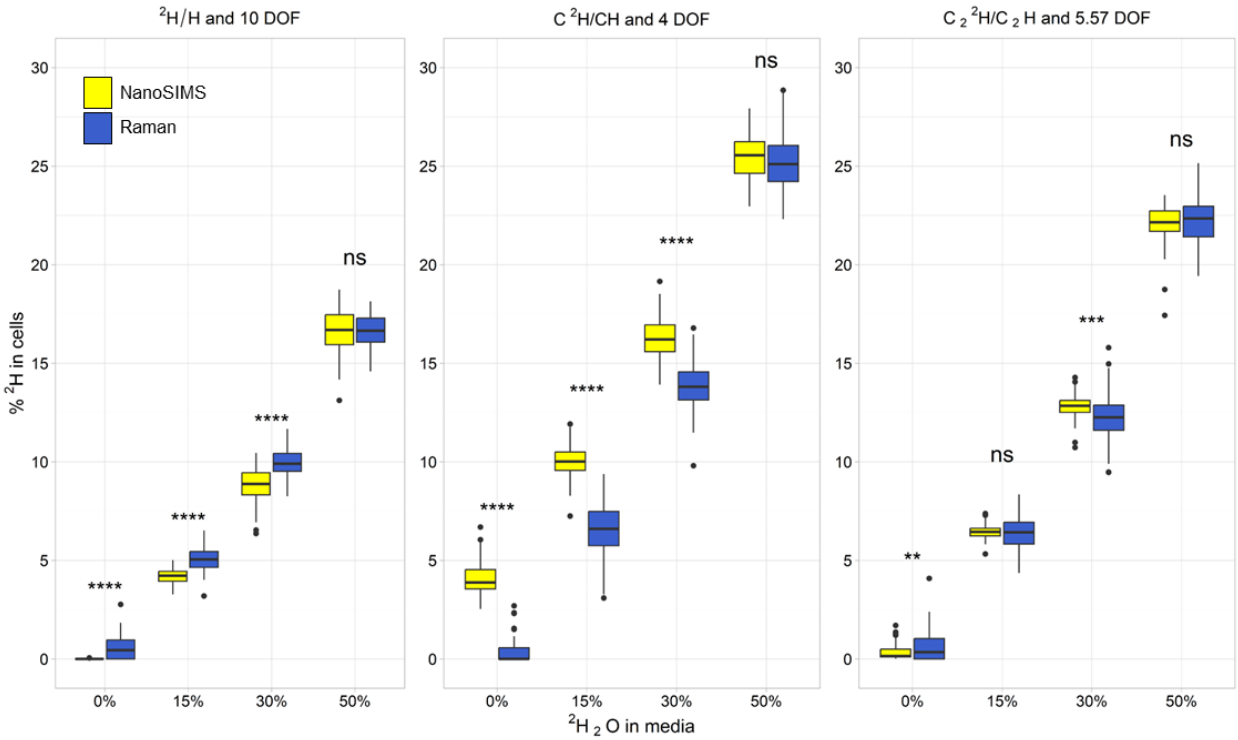

Fig. 4. Comparison of ^{2}H atom percent as measured by Raman using wavenumber ranges determined by DOF (see Table S4) compared to the three mass ratios measured using NanoSIMS. Using the wavenumber ranges deduced from the 2nd derivatives resulted in Raman data more closely resembling the NanoSIMS measurements for the ^{2}H/^{1}H and $C_2{}^2$H/$C_2{}^1$H mass ratios. All statistically significant differences are shown: *** = p-value < 1.0 x 10^{-3}, **** = p-value < 1.0 x10^{-10}, ns = not significant.

Conclusion

Single species microbial populations have been shown to exhibit metabolic heterogeneity, requiring analysis on a single cell level to differentiate phenotypes within the population (49-51). The application of SIP in conjunction with Raman or NanoSIMS is a common approach to studying nuanced physiological differences in populations (3, 12, 15) and for determining the metabolic activity of cells (14, 17, 52-54). However, a direct comparison of Raman and NanoSIMS for single cell SIP experiments using ^2H_2O at several different concentrations had never been performed. By quantifying the uptake of ^{2}H into the biomass of individual *E. coli* cells using correlative SIP-Raman-NanoSIMS we established the extent of data equivalence between the two techniques, thus improving the comparability of studies employing either Raman or NanoSIMS techniques.

To make the necessary comparison, several factors needed to be considered before datasets were compared. First, we investigated the efficacy of pre-processing methods for Raman data showing that for the model organism *E. coli*, truncation and various baselining methods have little impact on the calculation of ^{2}H in cells (Fig. S4 and S5). While these pre-processing methods had negligible influence on silent region of the spectra, it is likely that there would be a measurable effect on the fingerprint region of the spectra, highlighting the importance of testing the different pre-processing methods prior to data analysis (27). In addition to the comparison of pre-processing methods for Raman, we investigated the measurement of ^{2}H using different masses for NanoSIMS and found that ^{2}H measured in cells varies depending on the mass

analyzed (Fig. S8). As mentioned earlier, this could be due to a combination of sampling different ^{2}H populations associated with the cell, different IMF factors, and variable atomic mixing during the sputtering process (22). Measurements using $^{2}H/^{1}H$ mass ratio sample a portion of ^{2}H and ^{1}H sputtered by the primary beam, regardless of what it is bound to. However, measurements of $^{12}C^{2}H/^{12}C^{1}H$ and $^{12}C_2{}^{2}H/^{12}C_2{}^{1}H$ mass ratios mainly sample ^{2}H and ^{1}H that is specifically bound to ^{12}C, resulting in measurements of specific hydrogen pools within the cell. This could result in a selection bias against hydrogen bound to other atoms, such as nitrogen or oxygen, that are not proportionally measured. This same selection bias applies to measurements made using Raman, although Raman measures measure ^{2}H bound to various biomolecules.

Comparison of Raman and NanoSIMS data measuring the anabolic metabolism of ^{2}H in single cells revealed a high degree of similarity between the two techniques. This was supported by robust correlation coefficients for data analyzed using the canonical Raman wavenumber range for ^{2}H calculation as well as for those deduced using the 2nd derivative approach to calculating wavenumber ranges (Fig. 2 and S13). This finding supports the use of either Raman or NanoSIMS when analyzing cells incubated with $^{2}H_2O$, offering researchers flexibility in choosing the most suitable technique for their specific experimental requirements while allowing comparability to literature data. In hindsight, collecting additional biomass for isotope ratio mass spectrometry measurements for independent benchmarking could have improved our study.

The decision to use Raman versus NanoSIMS would necessarily depend on the nature of the experimental question. Modern Raman instruments can make measurements much more rapidly than NanoSIMS and the infrastructure cost is at least six times lower. Raman targets C-H bounds directly, which makes activity measurements relatively easy to interpret. For NanoSIMS analysis, $^{2}H/^{1}H$ measurements have very low detection limits enabling natural abundance measurements, despite having a relatively low electron affinity (0.75 V; (43)). Assuming 3 standard deviations for detection limits, the uncalibrated detection limit for the present experiment for NanoSIMS is 0.04 at% compared to >0.2% for Raman. However, NanoSIMS measurement targets all H in the cell including exchangeable H (*e.g.*, hydroxyl, amino, or thiol groups) as well as residual water; thus, careful thought concerning interpretation of results is necessary (25). The $^{12}C^{2}H/^{12}C^{1}H$ ion pair targets C-H bonds directly, but high background, presumably due to $^{12}C^{1}H_2$, prevents low detection limits at the high-transmission analysis conditions used here. An unknown amount of atomic recombination probably occurs (22) so some dilution of the $^{12}C_2{}^{2}H$ signal is possible. $^{12}C_2{}^{2}H/^{12}C_2{}^{1}H$ measurement can be performed at higher precision, but again recombination and background interferences limit detection and potentially accuracy. On the positive side, depending on enrichment levels, other peaks could be monitored along with either polyatomic pair to measure assimilation of other elements beside H (40). When lower detection limits than those afforded by $^{12}C^{2}H/^{12}C^{1}H$ or $^{12}C_2{}^{2}H/^{12}C_2{}^{1}H$ are required or the experiment requires the measurement of all cellular ^{2}H, we recommend that researchers consider using $^{2}H/^{1}H$, in addition to other mass ratios.

Our comparative investigation fills a critical void in the current understanding of spectroscopy and spectrometry techniques in microbiology and offers a foundation for the further exploration and application of SIP methods in diverse microbial systems. The comparability of Raman and NanoSIMS measurements of single cells presented in this study paves the way for a more nuanced and comprehensive understanding of microbial activities, interactions, and responses to isotopic labeling.

Materials and Methods

Preparation of isotopically labeled cells

Escherichia coli K12 (DSM498) cultures were grown aerobically at 200 rpm agitation at 37 °C for 13 h in M9 medium (0.38 mM thiamine and 22.2 mM glucose) that had been amended to a final concentration of either 0%, 15%, 30%, or 50% $^{2}H_2O$ (99.9%-^{2}H; Cambridge Isotope Laboratories). The optical density (600 nm) of the culture was measured every hour for the first six hours, after which measurements were taken every half hour. When the OD_{600} had reached 0.8-0.9, 1 mL of culture was sampled (Fig. S1) and chemically fixed by adding paraformaldehyde (PFA; Electron Microscopy Science; EM grade) to a final concentration of 2%. These samples were then incubated for 60 min at room temperature. Cells were then washed twice with 1× phosphate buffered saline (PBS; pH 7.4) by centrifugation at 16,000 g for 5 min, after which supernatants were removed, and cell pellets were resuspended in 1 mL of 1x PBS and samples stored at 4 ºC.

Preparation of stainless steel coupon

Fixed cells were dried to the surface of mirrored stainless steel due to its desired properties as a Raman substrate (55). The stainless steel coupon was prepared as previously described in Schaible *et al.* (24). Briefly, the coupon was cleaned by washing with a 1% solution of Tergazyme (Alconox, New York, NY) rinsed with Milli-Q water, subsequent one-minute washes in acetone and 200 proof ethanol, and then air dried. To maintain correct orientation of the samples, asymmetric boxes were etched into the mirrored surface of each coupon using a welder's pen (Fig. S2). 1 µL of each sample was spotted onto the coupon and air-dried at 46 °C for 1 min, after which the coupon was washed in 1:1 ethanol:MilliQ for 1 minute and then air dried. The coupon was incubated in a 300 nM (100 ng/mL) solution of DAPI (4',6-diamidino-2-phenylindole, ThermoFisher, Waltham, MA) for 3 minutes as per the manufacturer's instructions. The coupon was then rinsed three times in fresh PBS and then briefly dipped them into ice-cold Milli-Q water to remove salts and air-dried using compressed air. To track single cells across platforms, regions of interest (ROIs) were drawn around cells on the coupon using a Leica LMD6 Laser Microdissection System (Danaher Corporation, Washington DC) using a power setting of 7, a speed of 7, and aperture size of 7 (Fig. S3).

Confocal Raman microspectroscopy and spectral processing

Raman spectra of individual cells were acquired using a LabRAM HR Evolution Confocal Raman microscope (Horiba Jobin-Yvon) equipped with a 532 nm laser and 300 grooves/mm diffraction grating. The instrument was calibrated daily before use with a silica oxide standard. Cell spectra were acquired using a 100× dry objective (NA = 0.90) in the range of 250–3200 cm^{-1}, with 3 acquisitions of 10 s each, and a laser power of 4.5 mW. Spectra were processed using LabSpec version 6.5.1.24 (Horiba). The spectra were preprocessed in GNU R (56) using the Alkahest (57), ptw (58), and Pracma (59) packages. Each spectra was smoothed using the Savitsky-Goley algorithm, (30) followed by background subtraction and baselining of spectra using either asymmetric least squares (ALS) (31), polynomial fit (32), rolling ball (33), or statistics-sensitive non-linear iterative peak-clipping (SNIP) (34). Raman spectra baselined with the SNIP method were used for the comparison to the NanoSIMS data. Settings used for smoothing and baselining can be found in the R file deposited on GitHub (https://github.com/georgeschaible/Raman-spectra-processing). Each spectrum was then normalized to the sum of its absolute spectral intensity, and the incorporation of ^{2}H into biomass was calculated by $\left(\frac{^{12}C^{2}H}{^{12}C^{2}H+^{12}C^{1}H}\right) \times 100$, using the integration of the area under the curve (AUC) for the $^{12}C^{1}H$ (2800–3100 cm^{-1}) peak, the canonical $^{12}C^{2}H$ (2040–2300 cm^{-1}),

or the wavenumber ranges calculated using the 2nd derivative (Table S4). The AUC was calculated using the trapezoidal rule as follows: $AUC \approx \frac{h}{2}[\int(x_0) + 2\int(x_1) + 2\int(x_2) + \ldots + 2\int(x_n)]$ where h is the width of each interval, $\int x_i$ is the function value at each data point, and n is the number of data points.

Nano-scale secondary ion mass spectrometry

To map the elemental composition and the relative isotopic abundances of hydrogen, ion images of the same cells investigated by Raman were acquired using the Cameca 50L NanoSIMS at the Environmental Molecular Sciences Laboratory at Pacific Northwest National Laboratory in Richland, Washington. The vacuum gauge pressure in the analytical chamber during all analyses was consistently less than 3×10^{-10} mbar. Although no isotopic standards were available to calibrate the instrument for instrumental mass fractionation (IMF), similar responses between detectors were ensured by measuring an isotopic ratio. Electron multiplier voltages were set such that the maximum pulse height distribution (PHD) was at a discriminator voltage of -230 ± 10 mV. ^{1}H was used to set the PHDs for $^{2}H/H$ analyses and ^{28}Si- was used to set PHDs for C_2H/CH and $C_2{}^2H/C_2H$ measurements. Other analytical conditions included a 200 µm D1 aperture, 20 µm entrance slit, 250 µm aperture slit, and 100 µm exit slits. All NanoSIMS images were acquired using a 2 pA (~120 nm) 16 keV Cs^+ primary ion beam at 256 × 256-pixel resolution with a dwell time of 1 ms px^{-1}. Analysis areas were pre-sputtered with ~5×10^{15} ions cm^{-2} prior to collecting 15 consecutive frames. Secondary ions ($^{12}C_2$-, $^{12}C^1H$-, $^{12}C^2H^-$, $^{12}C_2{}^1H^-$, $^{12}C_2{}^2H^-$ or ^{1}H-, ^{2}H-) were accelerated to 8 keV and counted simultaneously using the EMs. Detectors collecting ^{2}H- and ^{1}H- ions were situated near the center of the magnet radius to improve simultaneous secondary centering characteristics, with careful attention paid to the secondary tuning of the Helmholtz coils to align ^{2}H and ^{1}H. After pre-sputtering, secondary signal was centered prior to collecting 15 consecutive frames for each image. The OpenMIMS plugin for ImageJ was used to correct images pixel by pixel, for dead time (44 ns) and Quasi Simultaneous Arrivals (QSA; $\beta = 0.5$), prior to aligning and summing the 15 frames. ROIs, of single microbes were acquired using the Bemsen algorithm in the Auto Local Threshold function on $^{12}C_2^-$ or ^{1}H summed images. We found that $^{2}H/^{1}H$ estimates were strongly influenced by ROI size due to a high H content in the stainless steel. Thus, attention was paid to the quality of the ROI-cell boundary. Data from single microbe ROIs were exported to a custom spreadsheet for data reduction. Internal uncertainties were obtained from counting statistics (44).

Statistical analyses

All datasets were analyzed in GNU R (56) using the tidyverse, rstatix, and ggpubr packages (60, 61). Statistical differences between multiple variables were determined using pairwise t-tests with a Bonferroni p-adjusted method. Calculations to determine the wavenumber range for ^{2}H used the pspline R package (62) and in-house written R code for the calculation of 2nd derivative inflection points of smoothed curves. All code used for analysis is deposited on GitHub (https://github.com/georgeschaible/Raman-spectra-processingd).

Data availability

Raman spectra have been deposited in the MicrobioRaman database under accession number S-MBRS8. NanoSIMS raw data is stored long-term on the EMSL data repository (search.emsl).

Author contributions

GS and RH designed the study. GS performed culturing and prepared samples for analysis. JAC collected the Raman spectra and GS analyzed the spectra. JBC and JB performed NanoSIMS analyses. GS and JBC compiled the data. JA and GS performed the second derivative calculations. GS performed the statistical analyses and prepared figures. GS and RH wrote the manuscript draft, which was then edited by all authors.

Acknowledgements

This study was funded through NIH award 1R35GM147166-01 to R.H. GS was partially supported by NASA FINESST fellowship 80NSSC20K1365. JAC was supported by NSF Research Traineeship Program award 2125748. Montana State University's Confocal Raman microscope was acquired with support by the NSF MRI program (DBI-1726561) and the M. J. Murdock Charitable Trust (SR-2017331). A portion of this research was performed under the Facilities Integrating Collaborations for User Science (FICUS) program (awards DOI: 10.46936/fics.proj.2020.51544/60000211) and used resources at the Environmental Molecular Sciences Laboratory (https://ror.org/04rc0xn13), which is a DOE Office of Science User Facilities operated under Contract No. DE-AC05-76RL01830. This manuscript has been authored by UT-Battelle, LLC, under contract DE-AC05-00OR22725 with the US Department of Energy (DOE). The US government retains and the publisher, by accepting the article for publication, acknowledges that the US government retains a nonexclusive, paid-up, irrevocable, worldwide license to publish or reproduce the published form of this manuscript, or allow others to do so, for US government purposes. DOE will provide public access to these results of federally sponsored research in accordance with the DOE Public Access Plan (https://www.energy.gov/doe-public-access-plan). We thank Hope McWilliams (MSU) for assistance with SIP labeling and Anthony Kohtz (MSU) for helpful input on the analysis of Raman spectra.

References

1. Hungate BA, Mau RL, Schwartz E, Caporaso JG, Dijkstra P, van Gestel N, Koch BJ, Liu CM, McHugh TA, Marks JC. 2015. Quantitative microbial ecology through stable isotope probing. Applied and environmental microbiology 81:7570-7581.
2. Berry D, Mader E, Lee TK, Woebken D, Wang Y, Zhu D, Palatinszky M, Schintlmeister A, Schmid MC, Hanson BT, Shterzer N, Mizrahi I, Rauch I, Decker T, Bocklitz T, Popp J, Gibson CM, Fowler PW, Huang WE, Wagner M. 2015. Tracking heavy water (D2O) incorporation for identifying and sorting active microbial cells. Proc Natl Acad Sci U S A 112:E194-203.
3. Hatzenpichler R, Krukenberg, V., Spietz, R.L., Jay, Z.J. 2020. Next-generation physiology approaches to study microbial community function at the single cell level. Nat Rev Microbiol.
4. Alcolombri U, Pioli R, Stocker R, Berry D. 2022. Single-cell stable isotope probing in microbial ecology. ISME Communications 2.
5. Neufeld JD, Wagner M, Murrell JC. 2007. Who eats what, where and when? Isotope-labelling experiments are coming of age. The ISME Journal 1:103-110.
6. Wegener G, Bausch M, Holler T, Thang NM, Prieto Mollar X, Kellermann MY, Hinrichs KU, Boetius A. 2012. Assessing sub-seafloor microbial activity by combined stable isotope probing with deuterated water and 13C-bicarbonate. Environmental microbiology 14:1517-1527.
7. Zhang X, Gillespie AL, Sessions AL. 2009. Large D/H variations in bacterial lipids reflect central metabolic pathways. Proceedings of the National Academy of Sciences 106:12580-12586.
8. Friedman I. 1953. Deuterium content of natural waters and other substances. Geochimica et cosmochimica acta 4:89-103.
9. Litvak I, Anker Y, Cohen H. 2018. On-line in situ determination of deuterium content in water via FTIR spectroscopy. RSC advances 8:28472-28479.
10. Lo H-Y, Wink K, Nitz H, Kästner M, Belder D, Müller JA, Kaster A-K. 2023. scMAR-Seq: a novel workflow for targeted single-cell genomics of microorganisms using radioactive labeling. Msystems 8:e00998-23.
11. Lee N, Nielsen PH, Andreasen KH, Juretschko S, Nielsen JL, Schleifer K-H, Wagner M. 1999. Combination of fluorescent in situ hybridization and microautoradiography—a new tool for structure-function analyses in microbial ecology. Applied and environmental microbiology 65:1289-1297.
12. Musat N, Musat F, Weber PK, Pett-Ridge J. 2016. Tracking microbial interactions with NanoSIMS. Curr Opin Biotechnol 41:114-121.
13. Harrison JP, Berry D. 2017. Vibrational spectroscopy for imaging single microbial cells in complex biological samples. Frontiers in microbiology 8:261878.
14. Musat N, Foster R, Vagner T, Adam B, Kuypers MM. 2012. Detecting metabolic activities in single cells, with emphasis on nanoSIMS. FEMS Microbiol Rev 36:486-511.
15. Lee KS, Landry Z, Pereira FC, Wagner M, Berry D, Huang WE, Taylor GT, Kneipp J, Popp J, Zhang M, Cheng J-X, Stocker R. 2021. Raman microspectroscopy for microbiology. Nature Reviews Methods Primers 1.
16. Cui L, Xin Y, Yang K, Li H, Tan F, Zhang Y, Li X, Zhu Z, Yang J, Kao SJ, Ren B, Zhu YG, Musat F, Musat N. 2023. Live tracking metabolic networks and physiological responses within microbial assemblages at single-cell level. PNAS Nexus 2:pgad006.
17. Wang Y, Huang WE, Cui L, Wagner M. 2016. Single cell stable isotope probing in microbiology using Raman microspectroscopy. Curr Opin Biotechnol 41:34-42.

18. Huang WE, Stoecker K, Griffiths R, Newbold L, Daims H, Whiteley AS, Wagner M. 2007. Raman-FISH: combining stable-isotope Raman spectroscopy and fluorescence in situ hybridization for the single cell analysis of identity and function. Environ Microbiol 9:1878-89.
19. Li Q, Chang J, Li L, Lin X, Li Y. 2023. Research progress of nano-scale secondary ion mass spectrometry (NanoSIMS) in soil science: Evolution, applications, and challenges. Sci Total Environ 905:167257.
20. Nuñez J, Renslow R, Cliff JB, Anderton CR. 2018. NanoSIMS for biological applications: current practices and analyses. Biointerphases 13.
21. Mcmahon G, Saint-Cyr HF, Lechene C, Unkefer C. 2006. CN− secondary ions form by recombination as demonstrated using multi-isotope mass spectrometry of 13 C-and 15 N-labeled polyglycine. Journal of the American Society for Mass Spectrometry 17:1181-1187.
22. Akse SP, Das G, Agustí S, Pichevin L, Polerecky L, Middelburg JJ. 2021. Imaging of organic signals in individual fossil diatom frustules with nanoSIMS and Raman spectroscopy. Marine Chemistry 228.
23. Eichorst SA, Strasser F, Woyke T, Schintlmeister A, Wagner M, Woebken D. 2015. Advancements in the application of NanoSIMS and Raman microspectroscopy to investigate the activity of microbial cells in soils. FEMS Microbiol Ecol 91.
24. Schaible GA, Kohtz AJ, Cliff J, Hatzenpichler R. 2022. Correlative SIP-FISH-Raman-SEM-NanoSIMS links identity, morphology, biochemistry, and physiology of environmental microbes. ISME Communications 2.
25. Caro TA, Kashyap S, Brown G, Chen C, Kopf SH, Templeton AS. 2023. Single-cell measurement of microbial growth rate with Raman microspectroscopy. bioRxiv:2023.12. 16.571966.
26. Bocklitz T, Walter A, Hartmann K, Rösch P, Popp J. 2011. How to pre-process Raman spectra for reliable and stable models? Analytica chimica acta 704:47-56.
27. Ryabchykov O, Guo S, Bocklitz T. 2018. Analyzing Raman spectroscopic data. Physical Sciences Reviews 4:20170043.
28. Gautam R, Vanga S, Ariese F, Umapathy S. 2015. Review of multidimensional data processing approaches for Raman and infrared spectroscopy. EPJ Techniques and Instrumentation 2:1-38.
29. Guo S, Popp J, Bocklitz T. 2021. Chemometric analysis in Raman spectroscopy from experimental design to machine learning–based modeling. Nature protocols 16:5426-5459.
30. Savitzky A, Golay MJ. 1964. Smoothing and differentiation of data by simplified least squares procedures. Analytical chemistry 36:1627-1639.
31. Eilers PH, Boelens HF. 2005. Baseline correction with asymmetric least squares smoothing. Leiden University Medical Centre Report 1:5.
32. Lieber CA, Mahadevan-Jansen A. 2003. Automated method for subtraction of fluorescence from biological Raman spectra. Applied spectroscopy 57:1363-1367.
33. Kneen M, Annegarn H. 1996. Algorithm for fitting XRF, SEM and PIXE X-ray spectra backgrounds. Nuclear Instruments and Methods in Physics Research Section B: Beam Interactions with Materials and Atoms 109:209-213.
34. Ryan C, Clayton E, Griffin W, Sie S, Cousens D. 1988. SNIP, a statistics-sensitive background treatment for the quantitative analysis of PIXE spectra in geoscience applications. Nuclear Instruments and Methods in Physics Research Section B: Beam Interactions with Materials and Atoms 34:396-402.
35. Matanfack GA, Pistiki A, Rosch P, Popp J. 2021. Raman (18) O-labeling of bacteria in visible and deep UV-ranges. J Biophotonics 14:e202100013.

36. Doughty DM, Dieterle M, Sessions AL, Fischer WW, Newman DK. 2014. Probing the subcellular localization of hopanoid lipids in bacteria using NanoSIMS. PloS one 9:e84455.
37. Kopf SH, McGlynn SE, Green-Saxena A, Guan Y, Newman DK, Orphan VJ. 2015. Heavy water and 15 N labelling with N ano SIMS analysis reveals growth rate-dependent metabolic heterogeneity in chemostats. Environmental microbiology 17:2542-2556.
38. Sáenz JP, Sezgin E, Schwille P, Simons K. 2012. Functional convergence of hopanoids and sterols in membrane ordering. Proceedings of the National Academy of Sciences 109:14236-14240.
39. Meyer NR, Fortney JL, Dekas AE. 2021. NanoSIMS sample preparation decreases isotope enrichment: magnitude, variability and implications for single-cell rates of microbial activity. Environ Microbiol 23:81-98.
40. Slodzian G, Wu T-D, Bardin N, Duprat J, Engrand C, Guerquin-Kern J-L. 2014. Simultaneous hydrogen and heavier element isotopic ratio images with a scanning submicron ion probe and mass resolved polyatomic ions. Microscopy and Microanalysis 20:577-581.
41. Bardin N, Duprat J, Slodzian G, Wu T-D, Baklouti D, Dartois E, Brunetto R, Engrand C, Guerquin-Kern J-L. 2015. Hydrogen isotopic fractionation in secondary ion mass spectrometry using polyatomic ions. International journal of mass spectrometry 393:17-24.
42. Goebbert DJ. 2012. Photoelectron imaging of CH−. Chemical Physics Letters 551:19-25.
43. Zhou J, Garand E, Neumark DM. 2007. Vibronic structure in C2H and C2D from anion slow electron velocity-map imaging spectroscopy. The Journal of chemical physics 127.
44. Fitzsimons IC, Harte B, Clark RM. 2000. SIMS stable isotope measurement: counting statistics and analytical precision. Mineralogical Magazine 64:59-83.
45. Hauri EH, Shaw AM, Wang J, Dixon JE, King PL, Mandeville C. 2006. Matrix effects in hydrogen isotope analysis of silicate glasses by SIMS. Chemical Geology 235:352-365.
46. Larsen TA, Goodsell DS, Cascio D, Grzeskowiak K, Dickerson RE. 1989. The structure of DAPI bound to DNA. Journal of Biomolecular Structure and Dynamics 7:477-491.
47. Wang Y, Xu J, Kong L, Liu T, Yi L, Wang H, Huang WE, Zheng C. 2020. Raman–deuterium isotope probing to study metabolic activities of single bacterial cells in human intestinal microbiota. Microbial biotechnology 13:572-583.
48. Ramsay J, Heckman N, Silverman B. 1997. Spline smoothing with model-based penalties. Behavior Research Methods, Instruments, & Computers 29:99-106.
49. Schreiber F, Ackermann M. 2020. Environmental drivers of metabolic heterogeneity in clonal microbial populations. Current opinion in biotechnology 62:202-211.
50. Schreiber F, Littmann S, Lavik G, Escrig S, Meibom A, Kuypers MM, Ackermann M. 2016. Phenotypic heterogeneity driven by nutrient limitation promotes growth in fluctuating environments. Nature microbiology 1:1-7.
51. Zimmermann M, Escrig S, Hubschmann T, Kirf MK, Brand A, Inglis RF, Musat N, Muller S, Meibom A, Ackermann M, Schreiber F. 2015. Phenotypic heterogeneity in metabolic traits among single cells of a rare bacterial species in its natural environment quantified with a combination of flow cell sorting and NanoSIMS. Front Microbiol 6:243.
52. Dekas A.E. PRS, Orphan V.J. 2009. Deep-Sea Archaea Fix and Share Nitrogen in Methane-Consuming Microbial Consortia. Science 326:422-426.
53. Fernando EY, McIlroy SJ, Nierychlo M, Herbst F-A, Petriglieri F, Schmid MC, Wagner M, Nielsen JL, Nielsen PH. 2019. Resolving the individual contribution of key microbial populations to enhanced biological phosphorus removal with Raman–FISH. The ISME journal 13:1933-1946.

54. Zhang M, Hong W, Abutaleb NS, Li J, Dong PT, Zong C, Wang P, Seleem MN, Cheng JX. 2020. Rapid determination of antimicrobial susceptibility by stimulated Raman scattering imaging of D2O metabolic incorporation in a single bacterium. Advanced Science 7:2001452.
55. Lewis AT, Gaifulina R, Isabelle M, Dorney J, Woods ML, Lloyd GR, Lau K, Rodriguez-Justo M, Kendall C, Stone N, Thomas GM. 2017. Mirrored stainless steel substrate provides improved signal for Raman spectroscopy of tissue and cells. J Raman Spectrosc 48:119-125.
56. Team RC. 2023. A langauge and environment for statistical computing, *on* http://R-project.org/. Accessed
57. Frerebeau N. 2023. alkahest: Pre-Processing XY Data from Experimental Methods. https://CRANR-projectorg/package=alkahest R package version 1.1.1.9000.
58. Bloemberg TG, Gerretzen J, Wouters HJ, Gloerich J, van Dael M, Wessels HJ, van den Heuvel LP, Eilers PH, Buydens LM, Wehrens R. 2010. Improved parametric time warping for proteomics. Chemometrics and Intelligent Laboratory Systems 104:65-74.
59. Borchers HW. 2023. pracma: Practical Numerical Math Functions https://CRANR-projectorg/package=pracma R package version 2.4.4.
60. McNamara A. 2018. Key attributes of a modern statistical computing tool. The American Statistician.
61. Kassambara A. 2019. Comparing groups: Numerical variables, vol 192. Datanovia.
62. Ramsey J, Ripley B. 2022. Package ‘pspline’. https://CRANR-projectorg/package=pspline R package version 1.0-19.

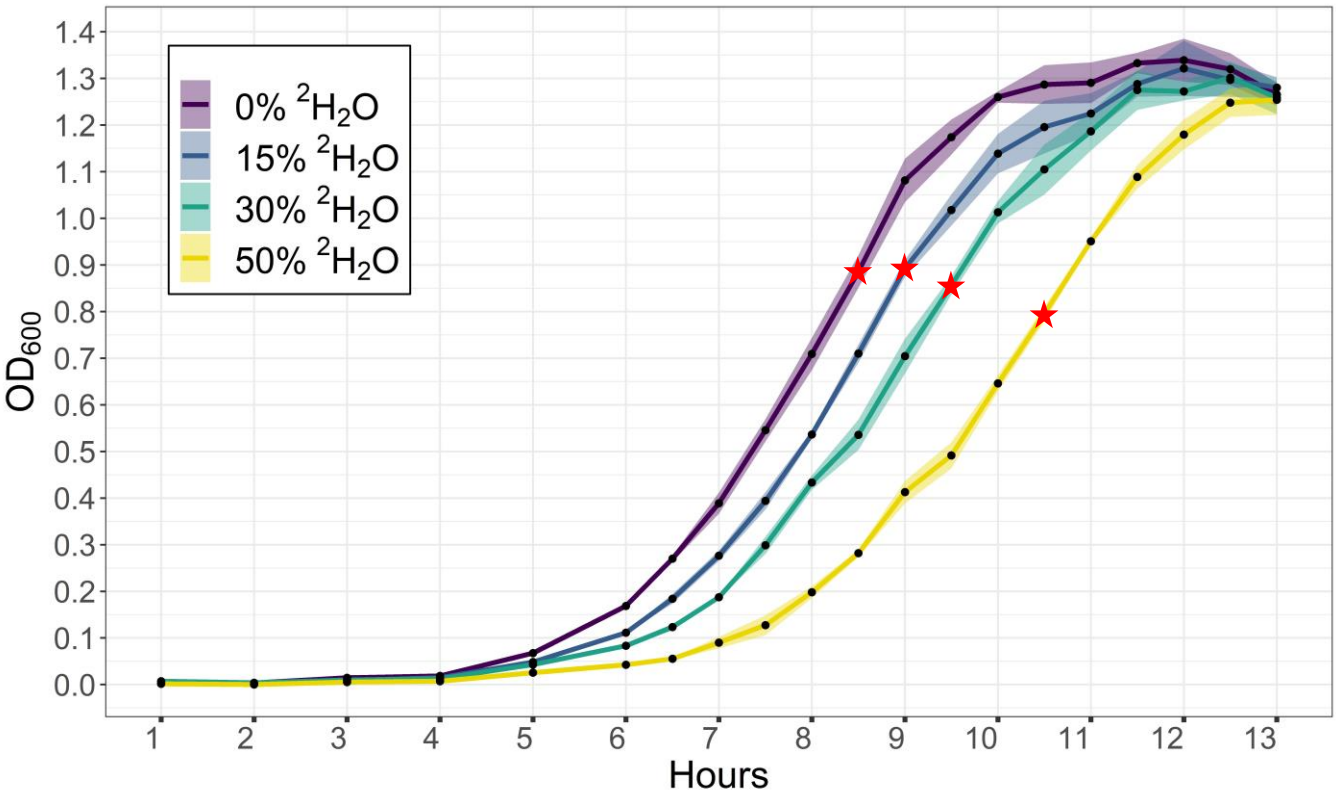

Fig. S1. Growth curves of triplicate *E. coli* cultures grown with varying ^2H_2O concentrations. Shaded region behind line shows the minimum and maximum OD_{600} of triplicate samples. Red stars highlight the time and OD_{600} at which cells were sampled and fixed for Raman and NanoSIMS analysis (harvesting at approximately same OD was attempted). The effect of ^2H_2O on *E. coli* growth can be seen by a delayed logarithmic growth upon the increased addition of heavy water to the growth media.

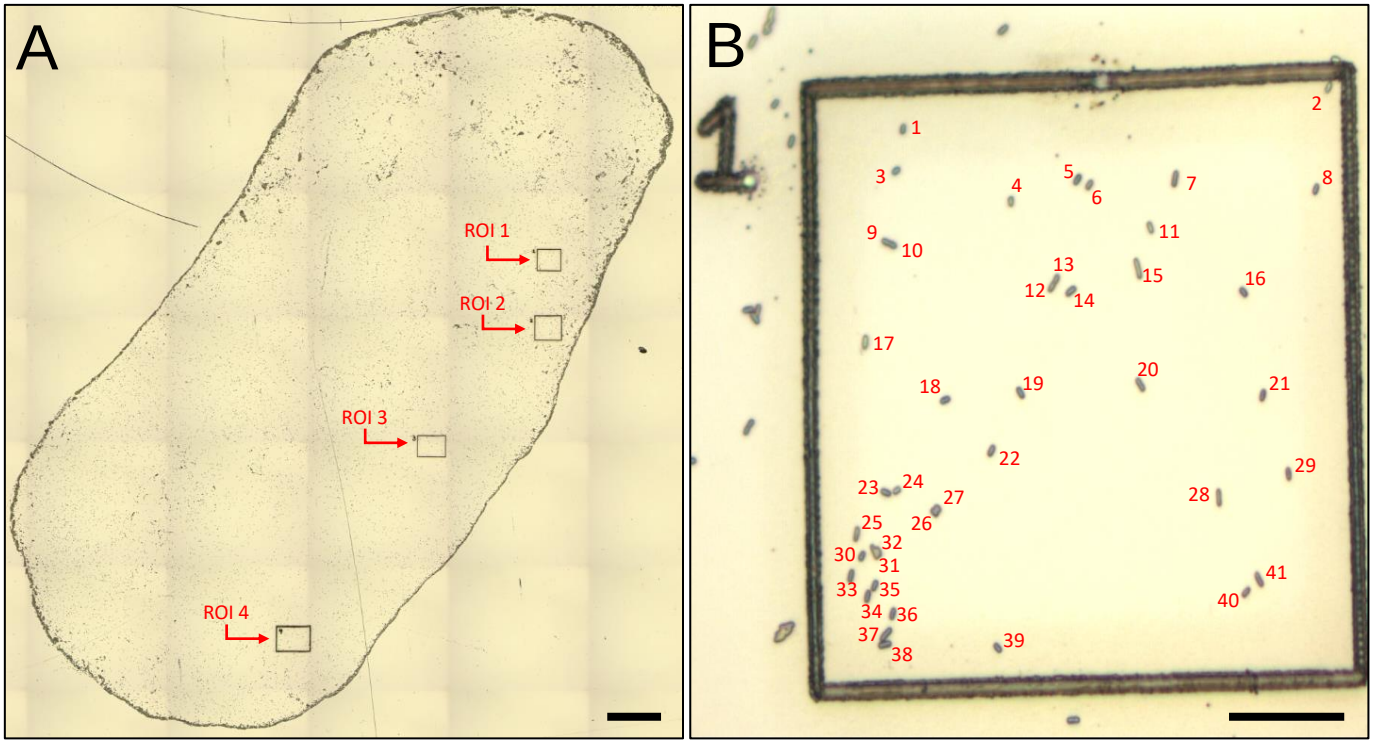

Fig. S2. Example of the mapping of ROIs and cells for correlative workflow. **A** Shows a tiled brightfield microscopy image of the individual ROIs etched into the surface of the stainless steel coupon using a laser microdissection microscope. Scale bar 100 µm. **B** Catalogued *E. coli* cells located within ROI 1 shown in A. Scale bar 10 µm.

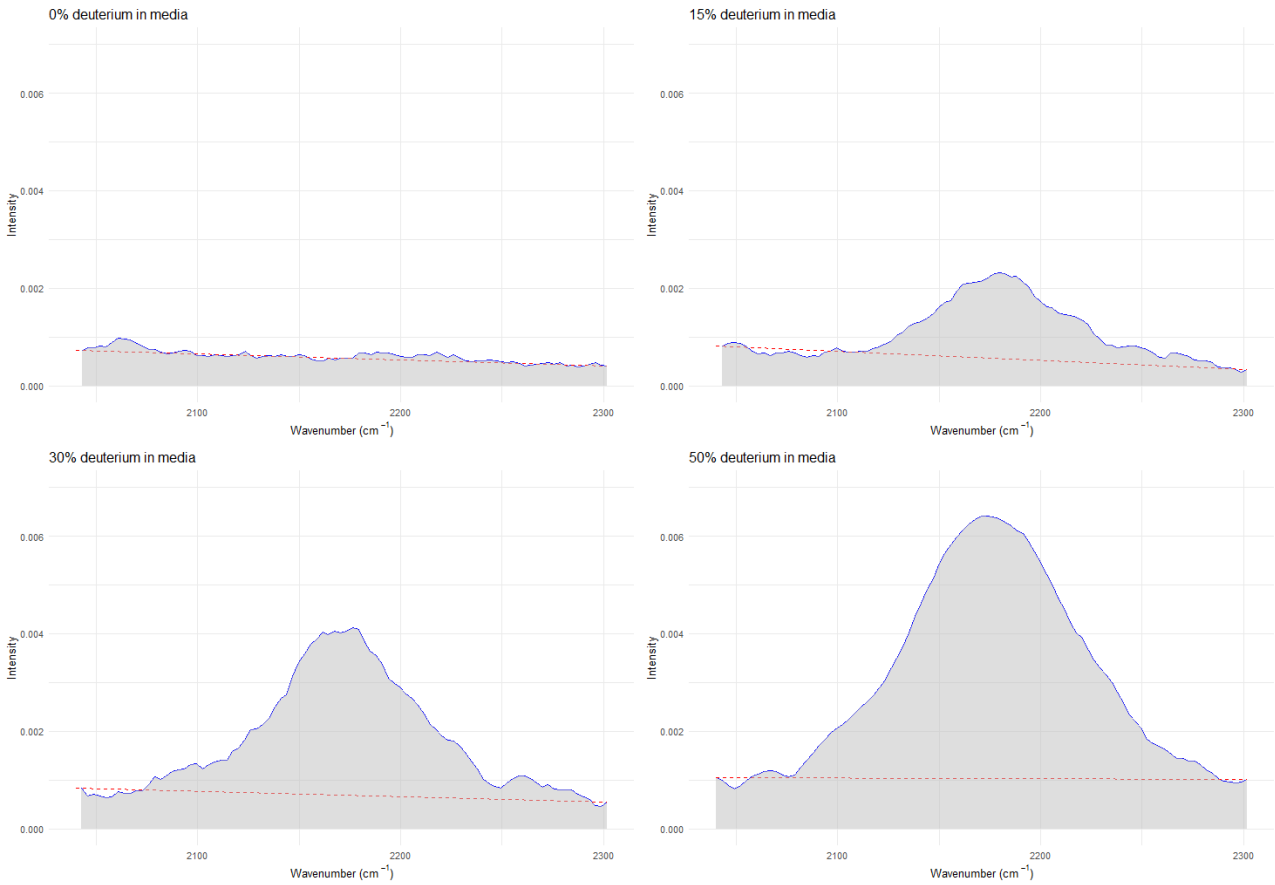

Fig. S3. Example showing the calculation of the AUC for ^{12}C-^{2}H. A baseline is drawn from the starting wavenumber (2,040 cm^{-1}) to the ending wavenumber (2,300 cm^{-1}) and only the area above that line and below the curve is calculated. The same method was applied to the ^{12}C-^{1}H peak (2,800-3,100 cm^{-1}).

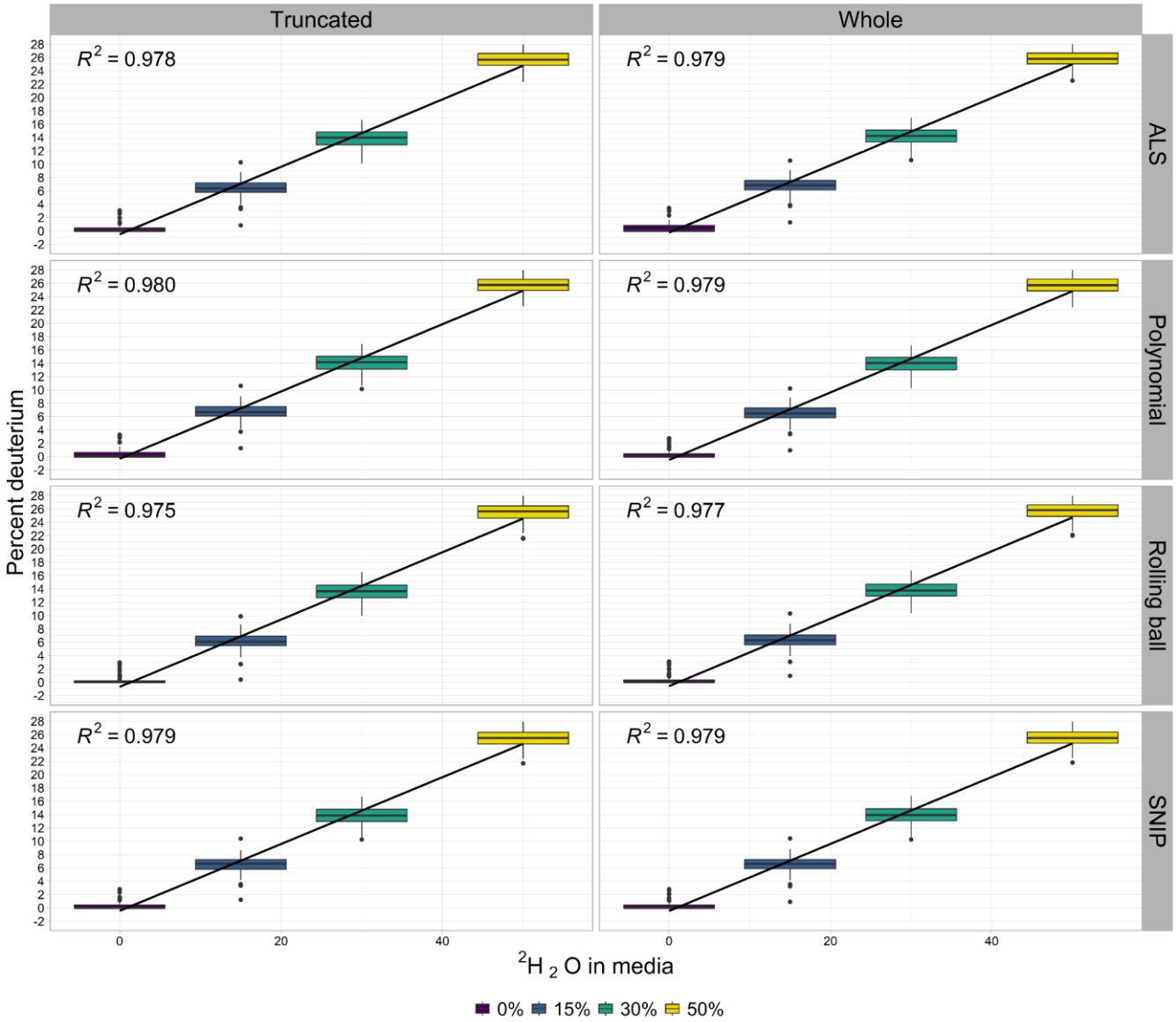

Fig. S4. Analysis of baselining methods for whole and truncated Raman spectra. The percent deuterium was calculated by comparing the ratio between CD and CH of the vibrational bands. Spectra were either analyzed as a whole (250-3,200 cm^{-1}) or truncated (1,800-3,200 cm^{-1}) with each of the four baselining methods. The analysis showed minimal differences between the baselining methods regarding the r-squared value for each of the concentrations of ^2H_2O in the media.

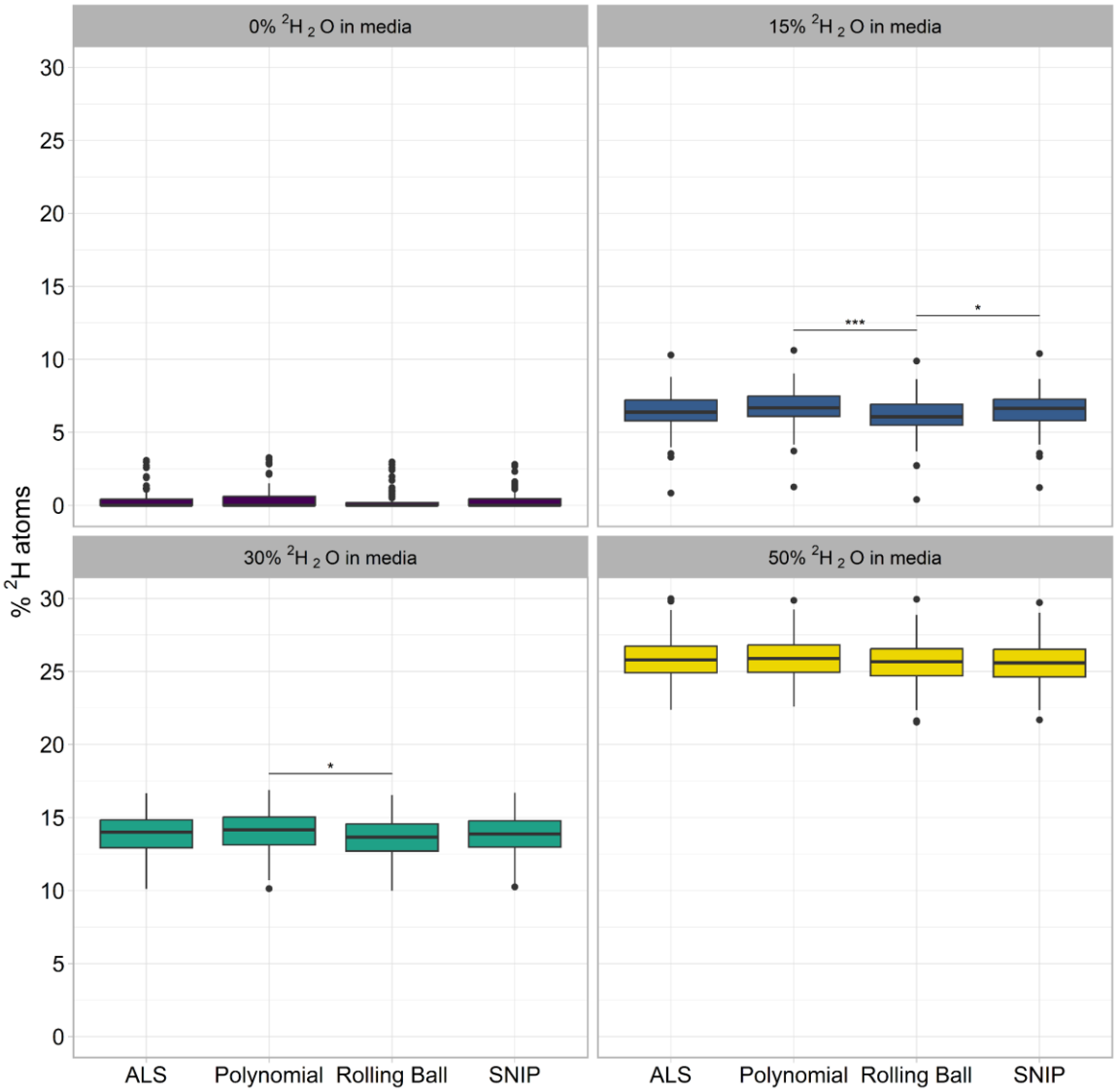

Fig. S5. Analysis of baselining methods for truncated Raman spectra. The percent deuterium was calculated by comparing the ratio between CD and CH of the vibrational bands. Spectra were either analyzed as a whole (250-3,200 cm^{-1}) or truncated (1,800-3,200 cm^{-1}) with each of the four baselining methods. Only rolling ball baselining method was statistically different as compared to other baselining methods at the 15% and 30% ^2H_2O incubations.

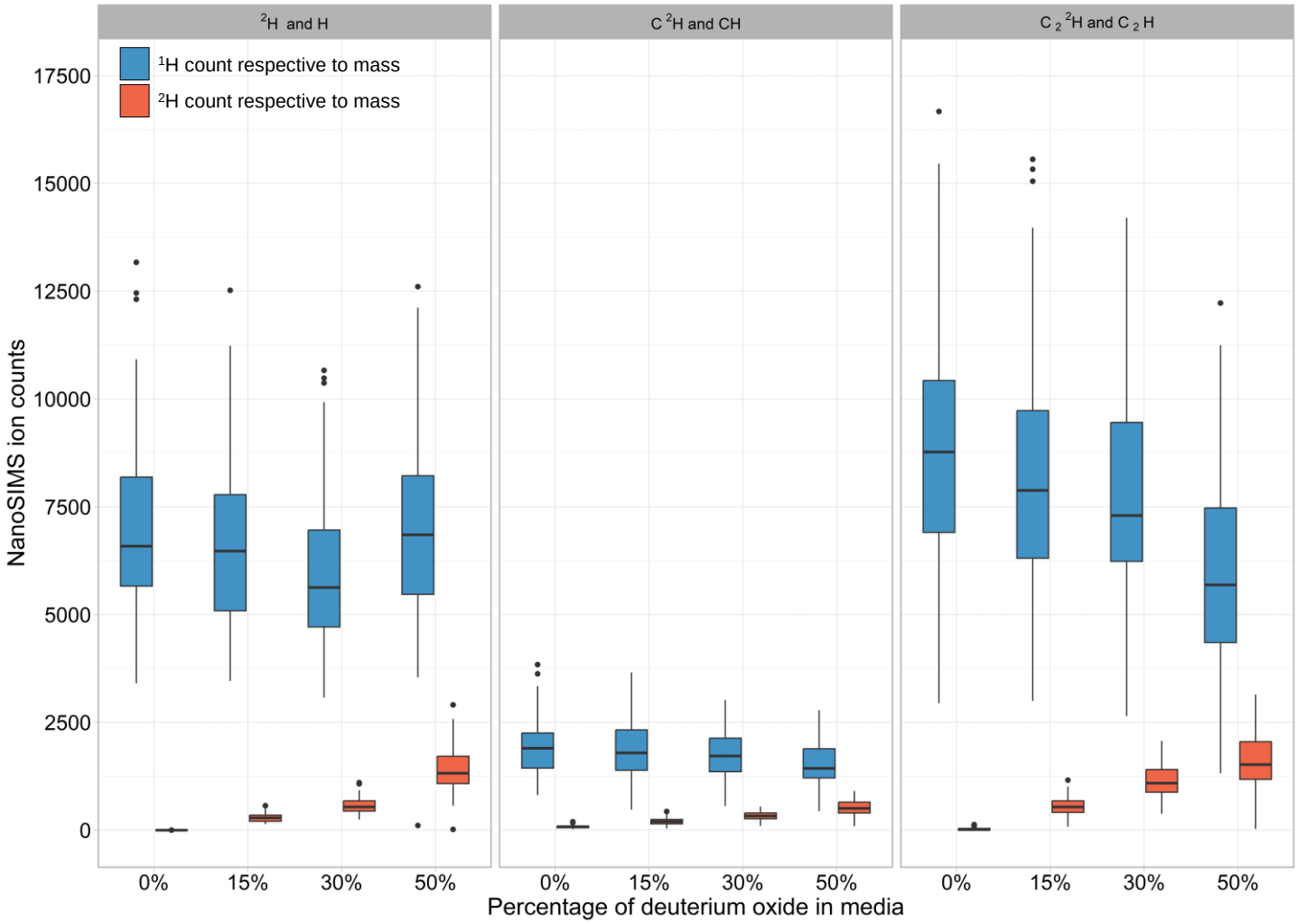

Fig. S6. Comparison of NanoSIMS ion counts for each ion mass analyzed. Blue bars show the mass measured for the H count and orange bars show the mass measured for the ^{2}H count, both respective to the mass ratio measured. Both C^2H/C^1H and $C_2{}^2H/C_2{}^1H$ were measured on the same cells, indicating that differences in counts are likely due to instrument drift or kinetic isotope/electron affinity effects.

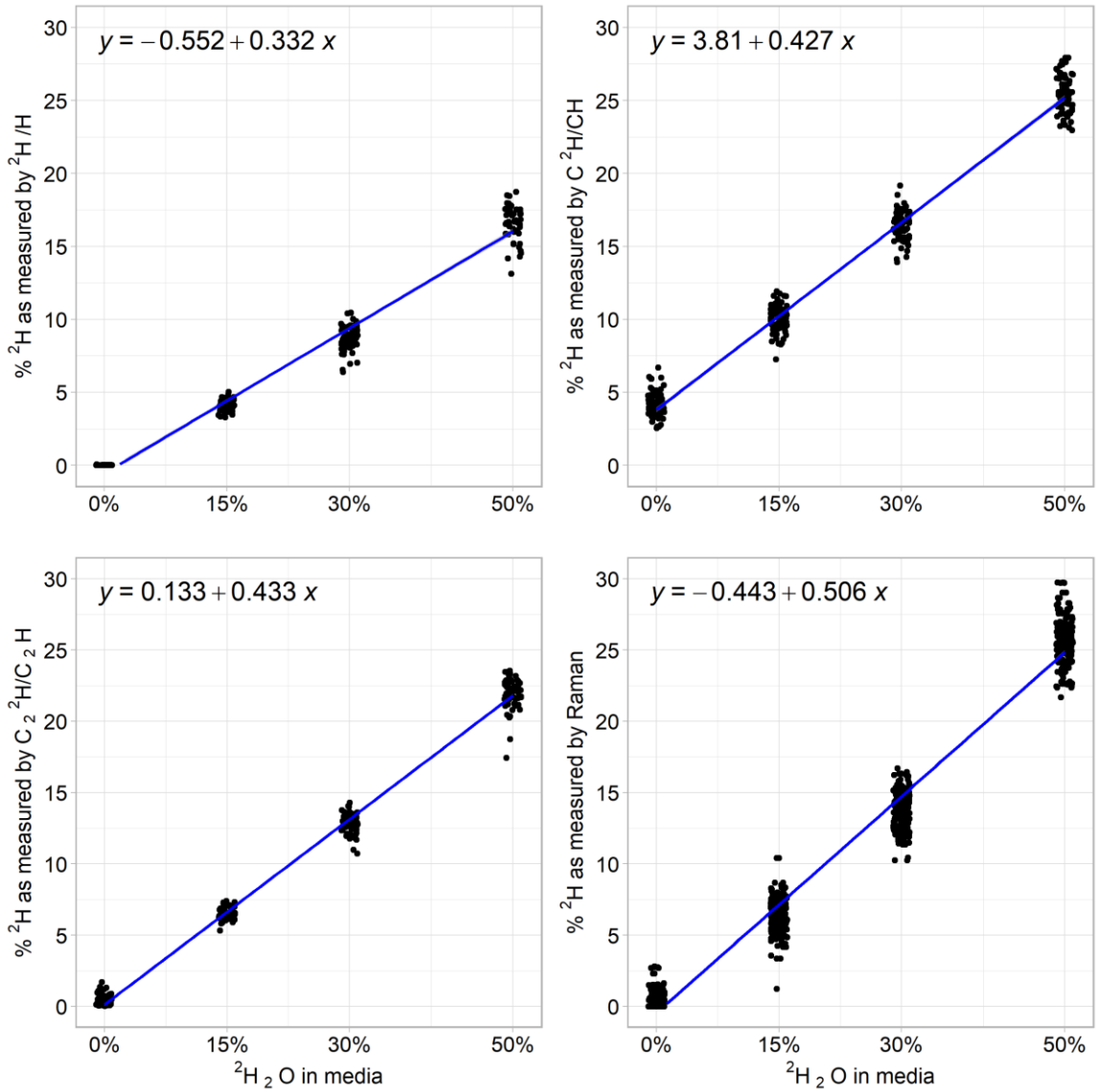

Fig. S7. Linear regressions showing the difference in slope for the ^{2}H content of cells measured using the three NanoSIMS masses and by Raman. Both $C^{2}H/C^{1}H$ and $C_2{}^{2}H/C_2{}^{1}H$ data was collected concurrently and have similar slopes. The $^{2}H/^{1}H$ was collected during a separate analytical session due to the need to adjust detectors for collection and thus cannot be directly compared to the $C^{2}H/C^{1}H$ and $C_2{}^{2}H/C_2{}^{1}H$ data.

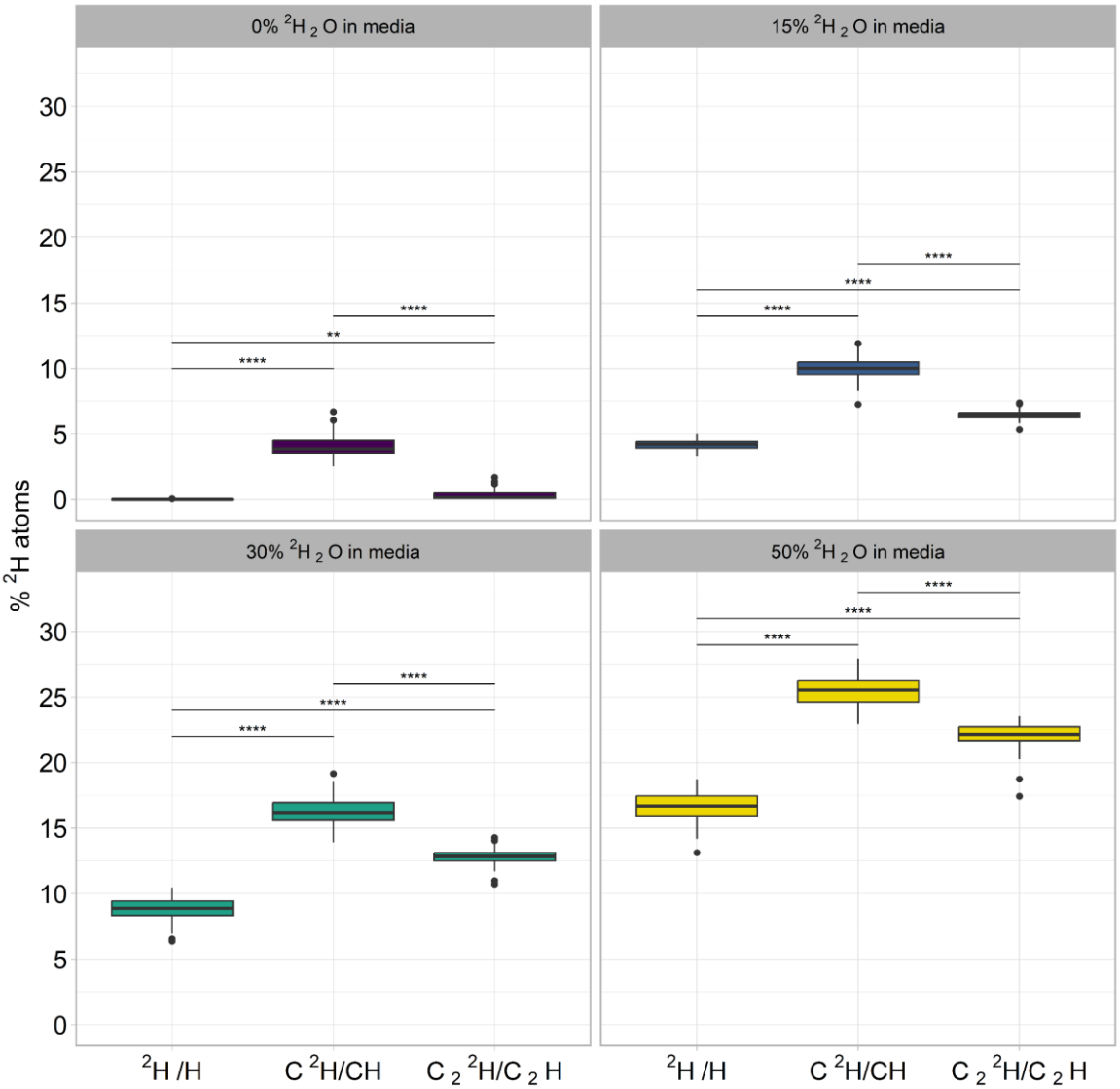

Fig. S8. Percent ^2H as measured by the different atomic mass ratios using NanoSIMS across the four heavy water incubations. All statistically differences are shown: ** = p-value < 5.0 x 10^{-3}, **** = p-value < 1.0 x10^{-10}.

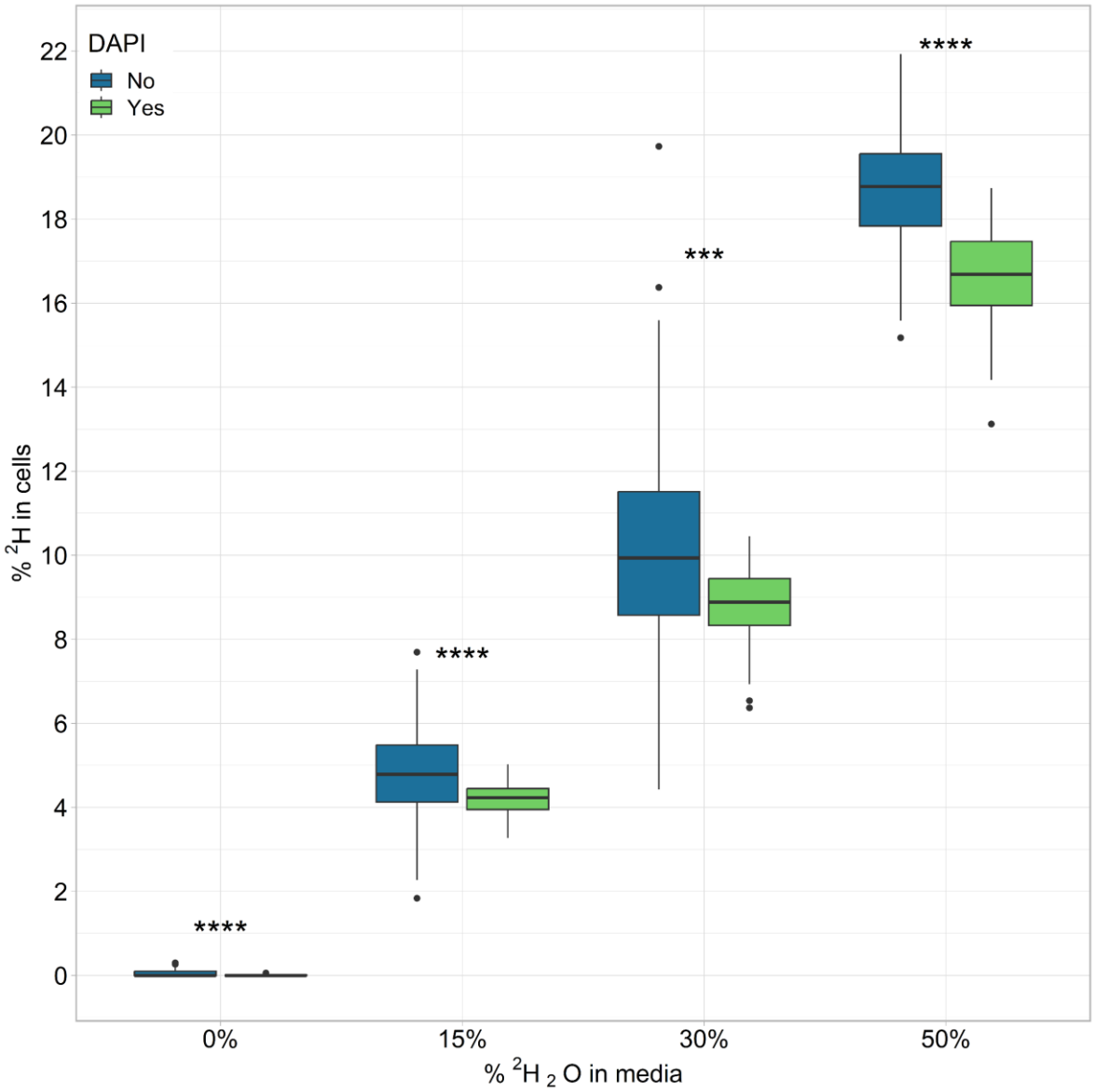

Fig. S9. NanoSIMS measurements of mass $^{2}H/H$ for *E. coli* cells either stained with DAPI or not. Cells that had not been stained with DAPI showed a statistically higher ^{2}H content than cells that had been treated with DAPI (*** = p-value < $1.0x10^{-4}$, **** = p-value < $1.0x10^{-5}$)

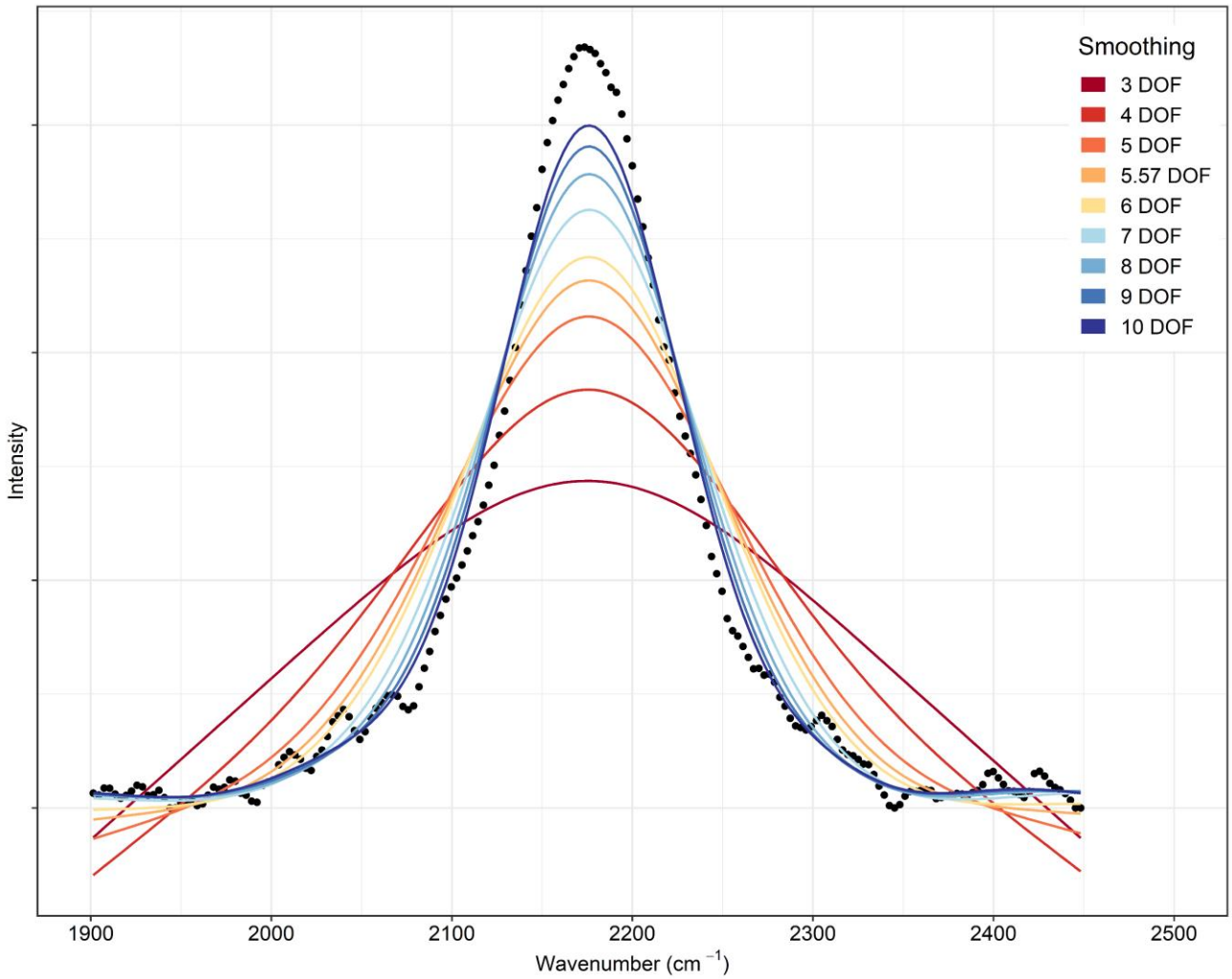

Fig. S10. Comparison of degrees of freedom (DOF) for the spline smoothing function of as applied to the $^{12}C^{2}H$ peak in a spectra obtained for a cell from the 50% $^{2}H_2O$ incubation. The higher the DOF, the better the fit to the data, but the further constrained the wavenumber range for the 2nd derivative becomes (see Figs S10 and S11).

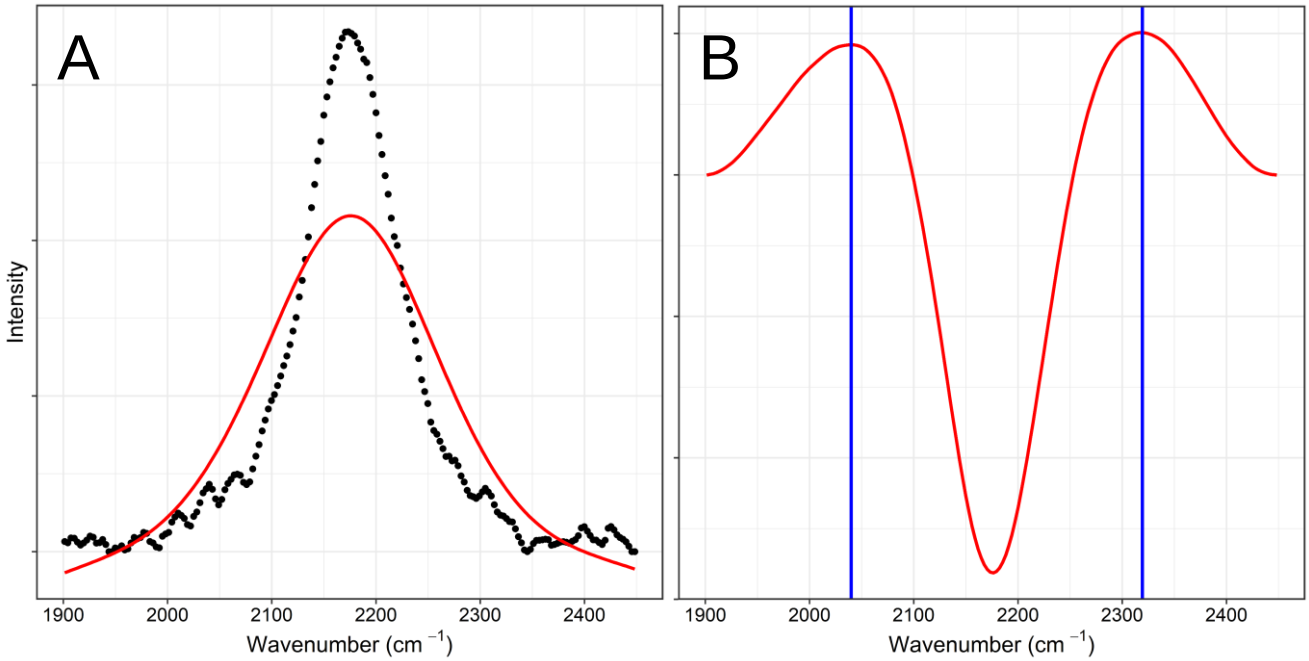

Fig. S11. Statistical evaluation of wavenumber range for 50% $^{2}H_{2}O$ incubation spectra. **A** Processed spectra (black dots) with five degrees of freedom (DOF) spline smoothing (red line). **B** Calculation of the 2nd derivative for the red line shown in panel **A**. The inflection points (blue vertical lines) are the max values of the curve on either side of the lowest value for the 2nd derivative of the curve and indicate the wavenumbers as determined by the 2nd derivative.

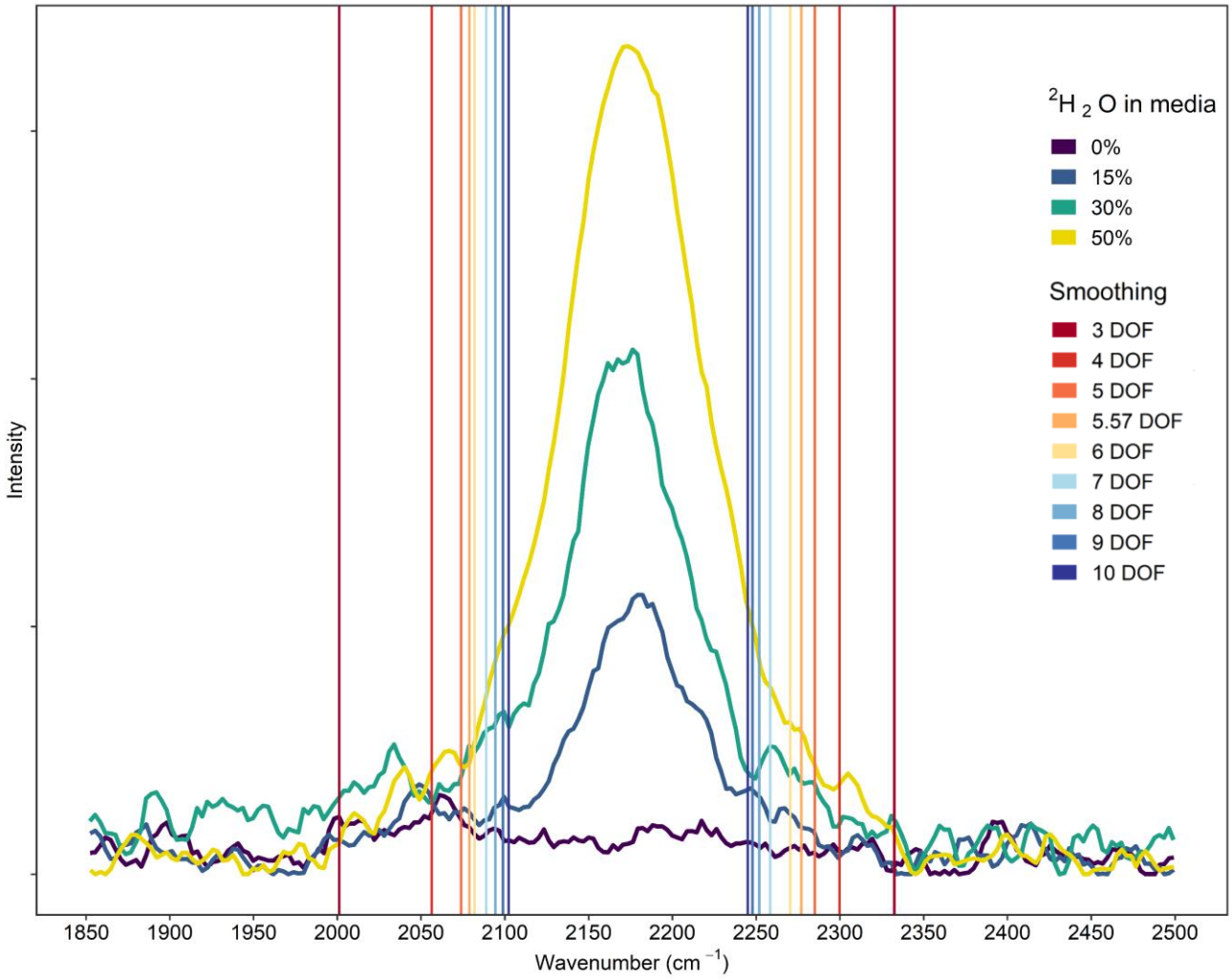

Fig. S12. Plot showing the wavenumber ranges (shown as vertical lines) as calculated by the 2nd derivative for the different degrees of freedom (DOF) smoothing. Example spectra for cells incubated in 0%, 15%, 30%, and 50% ^2H_2O are shown for reference.

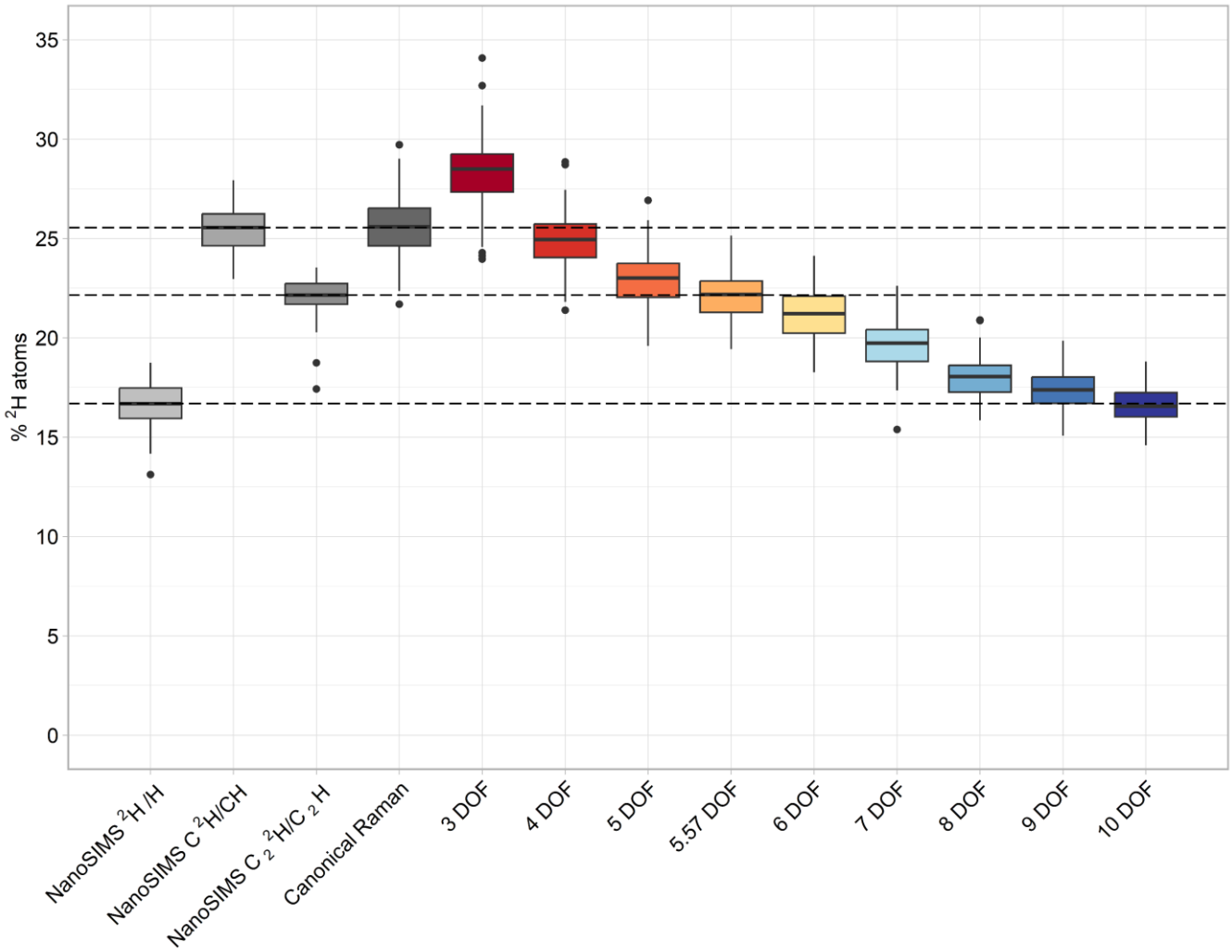

Fig. S13. Comparison of the atom percent of ^{2}H in cells from the 50% $^{2}H_2O$ incubation as determined by NanoSIMS and Raman analysis using the different wavenumber ranges calculated for the different degrees of freedom (DOF). Dashed horizontal lines indicate each DOF that best matches the respective NanoSIMS mass fraction.

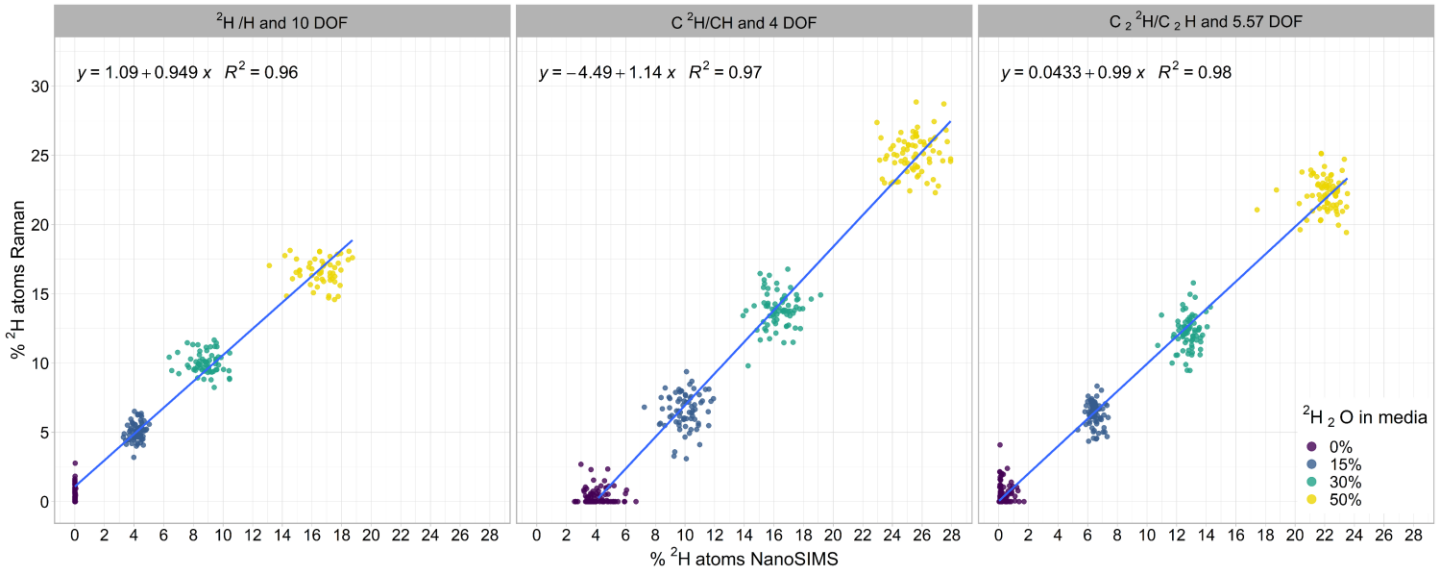

Fig. S14. Single cell comparison of the ^{2}H content of cells as measured by Raman using the 2nd derivative wavenumber ranges to NanoSIMS using specific mass ratios. Each dot represents a single cell analyzed with both techniques for different ^2H_2O concentrations in the culture medium. The linear model equation and fit (blue line) is shown for each comparison of Raman to NanoSIMS regarding the specific mass ratios.